Investigating vacancy cluster diffusion mechanisms in FeNiCr concentrated solid solution using the kinetic activation-relaxation technique

Md Mijanur Rahman [1,*] Gilles Adjanor,[2] Christophe Domain [2] and Normand Mousseau [3,†]

[1]*Département de génie physique, Institut Courtois et Regroupement québécois sur les matériaux de pointe, École Polytechnique de Montréal, C.P. 6079, Succ. Centre-Ville, Montréal, Québec H3C3A7, Canada*

[2]*Electricité de France, EDF Recherche et Développement, Département Matériaux et Mécanique des Composants, Les Renardières, F-77250 Moret sur Loing, France*

[3]*Département de physique, Institut Courtois et Regroupement québécois sur les matériaux de pointe, Université de Montréal, C.P. 6128, Succursale Centre-Ville, Montréal, Québec H3C 3J7, Canada*

(Received 17 October 2025; accepted 7 May 2026; published 27 May 2026)

A better understanding of the mechanisms of vacancy clustering and diffusion in concentrated solid solutions is essential to improve the design of alloys with enhanced radiation tolerance and thermal stability. In this study, the kinetic activation-relaxation technique (kART) was employed to investigate vacancy cluster behavior in FeNiCr CSAs at the atomistic level. By analyzing di-, tri-, and tetravacancy clusters, we reveal that cluster stability increases with size, driven by reduced formation energies, while local chemical composition—particularly Ni's stabilizing effect and Cr's role in enhancing mobility—influences defect evolution. By computing the diffusion barriers and entropic prefactors for more than 700 000 diffusion events, we find that divacancies combine notable stability with substantial mobility, while trivacancies exhibit significant mobility despite reduced stability, enabling efficient defect recombination through short-range migration mechanisms. In contrast, tetravacancies demonstrate greater stability but significantly restricted mobility, influencing localized defect interactions and microstructural evolution. These findings provide fundamental insights into the complex interplay between cluster size and local composition that affect both the enthalpic and entropic contributions to diffusion kinetics, offering a predictive framework for rationally designing alloy compositions to optimize radiation resistance and structural integrity in advanced nuclear and aerospace applications.

DOI: 10.1103/p14c-288d

I. INTRODUCTION

High-entropy alloys (HEAs) and concentrated solid-solution alloys (CSAs), distinguished by their multicomponent compositions with near-equiatomic proportions, represent a paradigm shift in materials design, offering exceptional mechanical properties, corrosion resistance, and stability under extreme conditions [1,2]. These attributes make them highly suitable for advanced applications, including nuclear reactors, aerospace components, and energy storage systems [3,4]. The performance of CSAs in such challenging environments—characterized by high temperatures, irradiation, or mechanical stress—is critically influenced by atomic-scale defects, particularly vacancy clusters, which drive microstructural evolution and mediate degradation mechanisms such as void swelling and defect accumulation [5,6]. A comprehensive understanding of the thermodynamic stability and kinetic behavior of these defects is essential for tailoring alloys to achieve superior durability and performance in demanding applications [7,8].

Vacancy clusters, ranging from divacancies to larger aggregates, play a pivotal role in the evolution of radiation-induced damage, influencing mass transport, defect recombination, and the formation of voids that undermine structural integrity [9,10]. The stability and mobility of these clusters are governed by their size and local chemical environment, which in CSAs is defined by the intricate interplay of multiple principal elements [11,12]. Unlike conventional alloys, the compositional complexity of CSAs introduces unique defect interactions, with specific elements modulating vacancy formation energies and migration barriers [13,14]. Despite growing interest in these materials, the microscopic mechanisms governing vacancy-cluster dynamics in multicomponent alloys remain incompletely understood, motivating the use of advanced atomistic simulation techniques.

Fe–Ni–Cr random solid solutions provide a well-established and technologically relevant model system for investigating defect behavior in multicomponent alloys. These alloys are known to form single-phase face-centered-cubic (fcc) or body-centered-cubic (bcc) structures over broad compositional ranges and constitute the base matrix of austenitic stainless steels used in nuclear and structural applications [5,6]. Their compositional flexibility allows systematic tuning of elemental concentrations, which has been reported to influence phase stability, mechanical response, oxidation behavior, and defect energetics. In particular, Ni stabilizes the fcc phase, while Cr contributes to oxidation resistance and modifies defect–solute interactions [4,11]. These characteristics make

*Contact author: md-mijanur.rahman@polymtl.ca
†Contact author: normand.mousseau@umontreal.ca

Fe–Ni–Cr–based CSAs a useful reference system for studying defect processes in chemically disordered alloys.

In the present work, we focus on a Fe–Ni–Cr solid solution with a bulk composition of 55% Fe, 28% Ni, and 17% Cr. This composition retains an Fe-dominant matrix representative of austenitic steels while incorporating sufficiently high Ni and Cr concentrations to stabilize the fcc structure and introduce pronounced chemical disorder. It lies within the Fe–Ni–Cr ternary space commonly used in atomistic studies of defect energetics and diffusion and has previously served as a reference system for investigations of monovacancy migration in chemically disordered Fe–Ni–Cr alloys [15,16]. The chemically random solid-solution character leads to a distribution of local atomic environments sampled by migrating defects, enabling correlations between local chemistry and vacancy-cluster energetics and kinetics to be examined within a controlled modeling framework.

To investigate vacancy-cluster dynamics in this chemically complex environment, we employ the kinetic activation–relaxation technique (kART), an advanced off-lattice kinetic Monte Carlo (KMC) method capable of capturing long-timescale atomistic processes [17–20]. The kART framework dynamically constructs an event catalog on the fly, enabling the exploration of complex diffusion pathways and long-range elastic interactions with high fidelity [21–23]. In addition, the use of harmonic transition state theory (hTST) allows for an explicit treatment of entropic contributions to the diffusion prefactor, yielding transition rates that reflect both energetic and vibrational effects associated with local atomic configurations [15,24,25]. This approach is particularly well suited for CSAs, where defect kinetics are strongly influenced by local chemical disorder.

In this study, we investigate the formation energy, migration pathways, and kinetic properties of vacancy clusters containing two to four vacancies in Fe–Ni–Cr concentrated solid solutions. Particular emphasis is placed on understanding how local chemical composition influences vacancy-cluster formation energies, migration barriers, prefactors, and effective mobilities. By resolving migration events at the atomic scale, this work provides detailed insight into the interplay between cluster size, chemical disorder, and defect kinetics in FeNiCr CSAs. These results contribute to a more comprehensive understanding of vacancy-mediated processes in chemically complex alloys and offer guidance for tailoring alloy compositions to improve performance in irradiation- and temperature-intensive environments.

II. METHODOLOGY

A. Kinetic activation-relaxation technique (k-ART)

The kinetic activation-relaxation technique (k-ART) is a self-learning kinetic Monte Carlo (KMC) algorithm designed to model atomic-scale dynamics over long timescales. It features on-the-fly construction of an event catalog and incorporates an exact treatment of elastic deformations. While comprehensive details of the implementation are available in the literature [18–20,26], we summarize the essential components of the method and outline the specific parameters employed in this study.

Each KMC step begins with a characterization of the local atomic environment. For every atom, a local connectivity graph is constructed using its neighbors within a 6.0 Å radius, where atomic connections are defined by a 2.7 Å cutoff. This graph is processed using the NAUTY algorithm [27], which assigns a unique topological identifier to the local environment, enabling rapid retrieval of associated events from the existing catalog. When an unknown topology is encountered, activation-relaxation technique nouveau (ARTn) [28–30] searches are initiated to discover new diffusion mechanisms. The event catalog is then dynamically updated with these new transitions.

After constructing the event tree, possible events are ranked according to their transition rates, given by

$$\Gamma_{ij} = \nu_0 \, e^{-\frac{E_b}{k_B T}}. \tag{1}$$

Here, ν_0 is the attempt frequency (prefactor), E_b is the activation energy (i.e., the energy difference between the transition state and the initial minimum), k_B is the Boltzmann constant, and T is the temperature. The prefactor ν_0 is computed using the harmonic transition state theory (hTST), originally developed by Vineyard [24],

$$\nu_{\mathrm{HTST}} = \frac{\prod_{i=1}^{3N} \nu_i}{\prod_{j=1}^{3N-1} \nu'_j}.$$

In this expression, ν_i are the vibrational frequencies at the initial state, and ν'_j are those at the transition state, excluding the single imaginary frequency. HTST accounts for vibrational entropy and variations in the attempt frequency, thereby enhancing the accuracy of KMC rate predictions over the standard approach where the prefactor is taken as constant [16,25].

To ensure accuracy in both local and nonlocal elastic effects, low-energy barriers undergo detailed relaxation. The refined transition rates are incorporated into the event tree, and the elapsed time for each KMC step is sampled from a Poisson distribution. To prevent the simulation from being trapped in low-barrier, nondiffusive states, the basin-autoconstructing mean-rate method (bacMRM) is employed [19,31]. This technique enables the algorithm to efficiently explore the energy landscape and accurately capture kinetic processes across a wide range of timescales.

B. Forcefields

In this study, we used the Bonny-2013 embedded-atom-method potential (EAM) [32], as implemented in LAMMPS, to simulate the FeNiCr alloy. This potential is specifically designed for analyzing radiation-induced defect formation and diffusion, capturing the interactions among multiple atomic species through pair potentials and embedding energy terms [16].

C. Simulation details

All simulations are performed in a 4000-atom cubic box (35.22 Å) with periodic boundary conditions, representing a FeNiCr solid solution with a bulk concentration of 55% Fe, 28% Ni, and 17% Cr. The system comprises a $10 \times 10 \times 10$

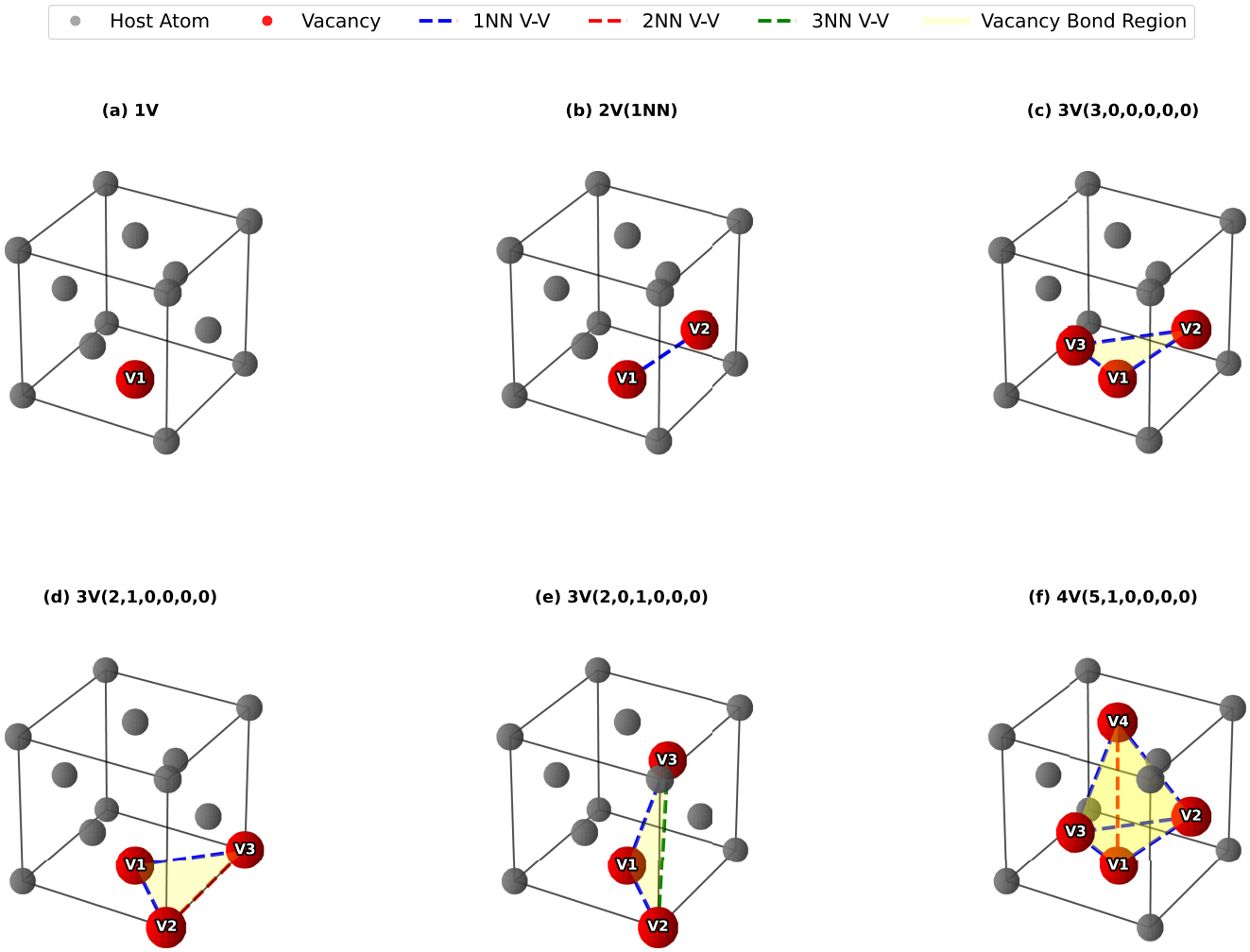

FIG. 1. Schematic representation of vacancy clusters in an FCC Fe-Ni-Cr concentrated solid-solution lattice. Host atoms are depicted as gray spheres, while vacancies are shown as red spheres labeled V1, V2, etc. Dashed blue lines indicate first-nearest-neighbor (1NN) vacancy–vacancy bonds, dashed red lines correspond to second-nearest-neighbor (2NN) vacancy–vacancy bonds, and dashed green lines correspond to third-nearest-neighbor (3NN) vacancy–vacancy bonds. The six panels illustrate distinct vacancy configurations: (a) 1V cluster consisting of a single isolated vacancy; (b) 2V(1NN) cluster with two vacancies as first-nearest neighbors; (c) 3V(3,0,0,0,0,0) cluster comprising three vacancies each separated by 1NN distances; (d) 3V(2,1,0,0,0,0) cluster containing two 1NN and one 2NN vacancy–vacancy pair separations; (e) 3V(2,0,1,0,0,0) cluster with two 1NN and one 3NN vacancy–vacancy pair separations; and (f) 4V(5,1,0,0,0,0) cluster featuring five 1NN and one 2NN vacancy–vacancy pair separations.

array of FCC unit cells (lattice parameter: 3.522 Å), containing 2200 Fe, 1120 Ni, and 680 Cr atoms.

Vacancy diffusion pathways are studied starting with configurations with two to four closely spaced vacancies. The systems are then relaxed at 0 K and 0 kPa to minimize internal pressure, followed by simulations at 600 K. Periodic boundaries and low vacancy concentration minimize vacancy–vacancy interactions, ensuring accurate diffusion rate evaluation.

Ten KMC simulations (1000–2500 steps each) are launched starting from different randomly generated configurations relaxed as stated above. The time evolution takes place using rates that include prefactors obtained within the harmonic transition state theory (hTST). These trajectories lead to 199 677, 225 491, and 306 374 generated events in total, with around 12 000, 15 000, and 18 000 selected steps for the divacancy, trivacancy, and tetravacancy cases, respectively, with a threshold of of up to 0.8 eV for the low-energy basins, depending on the trajectory. The total sets of events characterize the energy landscape, while selected events determine the system's kinetics and its dynamic evolution.

D. Vacancy structure notation

Vacancy configurations can be characterized in terms of vacancy-vacancy separation distances. Figure 1 illustrates representative examples of such clustering, following classification schemes established in previous studies of vacancy clusters in crystalline solids [21]. For an m-vacancy system, the number of possible vacancy pairs is given by

$$P(m) = \frac{m!}{2! \times (m-2)!}. \tag{2}$$

For example, a trivacancy complex (three vacancies) has $P(3) = 3$ unique pairs. The distance between vacancies can

be represented as d_i, where i indicates the nearest-neighbor (NN) order [21].

The configuration of an m-vacancy complex is then denoted as

$$mV\left(N_{d_1}, N_{d_2}, N_{d_3}, N_{d_4}, N_{d_5}, N_{d_6}\right), \tag{3}$$

where N_{d_i} represents the number of pairs with separation at the ith NN distance, including only the first six neighboring shells.

As shown in Fig. 1, specific configurations include compact and extended vacancy clusters depending on the distribution of pair separations. For example, $3V$ (2, 1, 0, 0, 0, 0) describes a trivacancy configuration with two pairs at the first-nearest-neighbor distance and one pair at the second-nearest-neighbor distance [see Fig. 1(d)]. This notation effectively captures the spatial arrangement and binding characteristics of vacancy complexes.

E. Formation energy calculation

The formation energy per vacancy (E_f) quantifies the energy change associated with creating a defect in a material and is calculated as

$$E_f = \left(E_{\text{defect}} + \sum_i k_i \mu_i - \bar{E}_{\text{perfect}}\right) \Big/ N_{\text{defect}}, \tag{4}$$

where E_{defect} is the total energy of the defective structure, k_i is the number of atoms of the ith species removed ($k_i <= 0$), μ_i is the chemical potential of the ith species, $\bar{E}_{\text{perfect}}$ is the average energy of the perfect lattice, and N_{defect} is the total number of defects in the system, $N_{\text{defect}} = \sum_i k_i$.

Because vacancies diffuse in a random solid solution, it is not possible to define a unique configuration that serves as a reference energy point. Instead, it is necessary to evaluate the defect formation energy for each configuration along the trajectory with respect to a potential reference system where vacancies are replaced by the atomic species initially removed; when multiple vacancies are involved, this reference is not unique. The procedure we retain here is the following: to calculate $\bar{E}_{\text{perfect}}$, the removed atoms are reintroduced into the structure to ensure the correct reference configuration; each possible atomic arrangement is explored by performing permutations to minimize energy and accurately reflect the system symmetry, and the reference energy is defined as the average energy of these defect-free fully relaxed configurations.

F. Calculation of cluster lifetime and effective diffusion coefficient

As obtaining lifetime and mobility for vacancy clusters directly from kART simulations would require computational resources beyond practical limits—particularly because of the large variability of local chemical environments—we adopt a mean-field Markov chain framework. This approach neglects explicit spatial and chemical correlations while retaining mechanism-specific kinetic statistics derived from atomistic sampling.

For each migration mechanism, kART simulations provide a distribution of activation barriers arising from distinct local atomic environments. In the harmonic transition state theory (hTST) framework, each sampled barrier $E_b^{i\to j}$ is converted into a transition rate using its mechanism-specific vibrational prefactor,

$$\Gamma_{i\to j} = \nu_{\text{hTST}}^{i\to j} \exp\left(-\frac{E_b^{i\to j}}{k_B T}\right), \tag{5}$$

where $\nu_{\text{hTST}}^{i\to j}$ is the mechanism-specific prefactor obtained from atomistic calculations. This procedure generates a rate distribution in rate space for each mechanism. The mean transition rate and its standard deviation (σ) are then calculated from this distribution. Markov chain simulations are performed using (i) the mean rate and (ii) the mean rate $\pm 1\sigma$, allowing us to quantify the sensitivity of transport properties to local chemical fluctuations.

A transition matrix is constructed to track the evolution of a vacancy cluster from its ground state through all intermediate configurations until one vacancy migrates beyond the fourth-nearest-neighbor (4NN) distance, which defines cluster dissociation. At each step of the Markov chain, a transition to a new state k is selected probabilistically according to the transition probabilities p_{ik}. The residence time of a bound cluster (xV, with $x = 2, 3, 4$) is updated stochastically as

$$\tau_i^{x\text{V}} = \tau_{i-1}^{x\text{V}} - \frac{\ln(\mu)}{\sum_k \Gamma_k}, \tag{6}$$

where $\mu \in (0, 1]$ is a uniformly distributed random number and $\sum_k \Gamma_k$ represents the total escape rate from the current state. This procedure is repeated until a vacancy escapes beyond the 4NN distance, thereby defining the cluster lifetime. Statistical convergence is ensured by performing $N_{\text{sim}} = 5 \times 10^6$ independent realizations.

The effective diffusion coefficient of a vacancy cluster is then obtained from the accumulated statistics as

$$D_{\text{eff}}^{x\text{V}} = \frac{1}{N_{\text{sim}}} \sum_{i=1}^{N_{\text{sim}}} \frac{R_i^2}{6\tau_i}, \tag{7}$$

where R_i^2 is the squared displacement of the cluster center of mass prior to dissociation and τ_i is the total lifetime in simulation i.

We emphasize that $D_{\text{eff}}^{x\text{V}}$ represents an *effective cluster mobility* over its finite lifetime rather than a macroscopic tracer diffusion coefficient. Because long-time spatial and chemical correlations typical of concentrated alloys are not explicitly resolved in the mean-field treatment, this formulation provides a controlled, mechanism-based comparison of relative cluster mobilities across different kinetic models while systematically incorporating the statistical spread of atomistic transition rates.

For benchmarking purposes, a constant-prefactor model is introduced using a fixed attempt frequency $\nu_0 = 10^{13}$ Hz. Each sampled barrier from the same barrier distribution is converted into a rate according to

$$\Gamma_{i\to j} = \nu_0 \exp\left(-\frac{E_b^{i\to j}}{k_B T}\right). \tag{8}$$

This generates a corresponding rate distribution in rate space, from which the mean and standard deviation are evaluated.

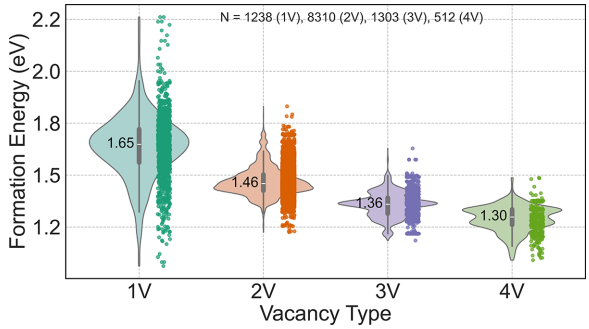

FIG. 2. Distribution of formation energies per vacancy for the most dominant configurations of 1V–4V vacancy clusters: 1V, 2V(1NN), 3V(3,0,0,0,0,0), and 4V(5,1,0,0,0,0) (schematics in Fig. 1). Violin plots with embedded boxplots depict the spread and quartiles of formation energies for each vacancy type, with individual data points overlaid to highlight the density of the distribution. Median values are indicated by the boxplots. The sample sizes are 1238 for 1V, 8310 for 2V, 1303 for 3V, and 512 for 4V vacancy clusters.

The Markov chain then employs the mean rate and mean $\pm 1\sigma$ values, ensuring a statistically consistent and direct comparison between the hTST-based and constant-prefactor kinetic frameworks.

III. RESULTS

A. Stability of vacancy clusters

The energetic stability (as quantified by formation energies) of vacancy clusters in FeNiCr concentrated solid solutions (CSAs) depends strongly on both cluster size and the surrounding local chemical environment. As shown in Fig. 2, the formation energy per vacancy decreases monotonically with increasing cluster size: from 1.65 eV for monovacancies, to 1.46 eV for divacancies, 1.36 eV for trivacancies, and 1.30 eV for tetravacancies. This trend reflects an energetic preference for vacancy aggregation, whereby clustering lowers the overall system internal energy. Such size-dependent reductions in formation energy are consistent with prior observations in other alloy systems, including dilute Fe–Cr–Ni alloys and copper, where vacancy clustering enhances defect stability and influences microstructural evolution under irradiation [33].

Figure 3 illustrates the formation-energy distribution of divacancy configurations across the first six-nearest-neighbor (NN) separations. The first-nearest-neighbor (1NN) configuration is both the most energetically favorable and the most statistically prevalent, with over 8000 sampled occurrences and a median formation energy of 1.46 eV. Configurations involving second-nearest-neighbor (2NN) and more distant separations exhibit significantly higher formation energies. The plateau observed beyond approximately the third-nearest-neighbor separation is consistent with the rapid decay of elastic interactions between two dilatational point defects once their elastic coupling becomes negligible. These trends indicate a strong energetic preference for compact vacancy clustering and are consistent with positron annihilation studies in quenched FeCrNi alloys, which report similar growth and stability of vacancy clusters at moderate temperatures [34].

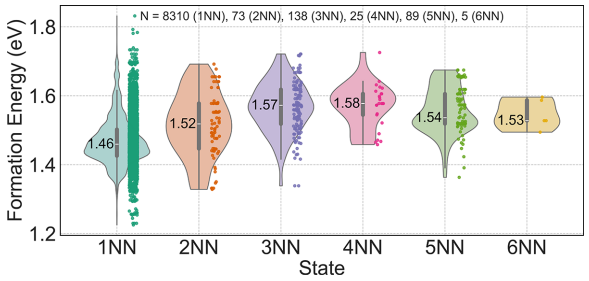

FIG. 3. Distribution of formation energies per vacancy for the first six-nearest-neighbor (NN) configurations or states for divacancies in FeNiCr concentrated solid-solution alloys: Violin plots with embedded boxplots illustrate the spread and quartiles of formation energies for each state. Individual data points are overlaid to show data distribution density. Median values are indicated by the boxplots. Sample sizes are 8310 for 1NN, 73 for 2NN, 138 for 3NN, 25 for 4NN, 85 for 5NN, and 5 for 6NN divacancy configurations.

To explore the influence of local chemical environments, Figures 4–6 present correlations between formation energy and atomic concentrations of Fe, Ni, and Cr within the first nearest-neighbor shell around the vacancy pair (1NN), the second nearest-neighbor shell including all atoms within that coordination range (2NN), and the subset of second-nearest-neighbor atoms not shared with the 1NN shell of either vacancy (2NN-only) for selected divacancy, trivacancy, and tetravacancy configurations. A pronounced negative correlation is observed between local Ni content and vacancy formation energy across all cluster types and shell distances, indicating that Ni-rich regions energetically favor vacancy clustering. This stabilizing effect of Ni is in agreement with density functional theory (DFT) studies, which demonstrates that Ni lowers the formation energy of vacancies in both random-concentrated and paramagnetic austenitic Fe-Cr-Ni alloys [13,14]. In contrast, Fe shows a consistent positive correlation with formation energy, indicating that Fe-rich environments are less favorable for vacancy clustering. Cr plays a dual role: while it may contribute to local strain relief in small clusters, it generally destabilizes larger vacancy configurations, as reflected in a weaker or positive correlation between Cr content and formation energy. This behavior has also been reported in DFT studies, which found increased vacancy formation energies with higher Cr content in Fe-Cr-Ni systems [14,35]. Quantitative compositional analysis (Table I) further supports these trends. Ni is consistently enriched near

TABLE I. Chemical composition within the first-nearest-neighbor shell surrounding the vacancy clusters.

Configuration	Fe (%)	Ni (%)	Cr (%)
Bulk system	55.00	28.00	17.00
1V	38.00	43.00	19.00
2V(1NN)	46.64	35.95	17.41
3V(3,0,0,0,0,0)	48.88	32.51	18.61
3V(2,1,0,0,0,0)	46.80	32.78	20.42
3V(2,0,1,0,0,0)	39.22	42.30	18.48
4V(5,1,0,0,0,0)	53.82	31.08	15.10
4V(5,0,1,0,0,0)	54.56	32.27	13.17

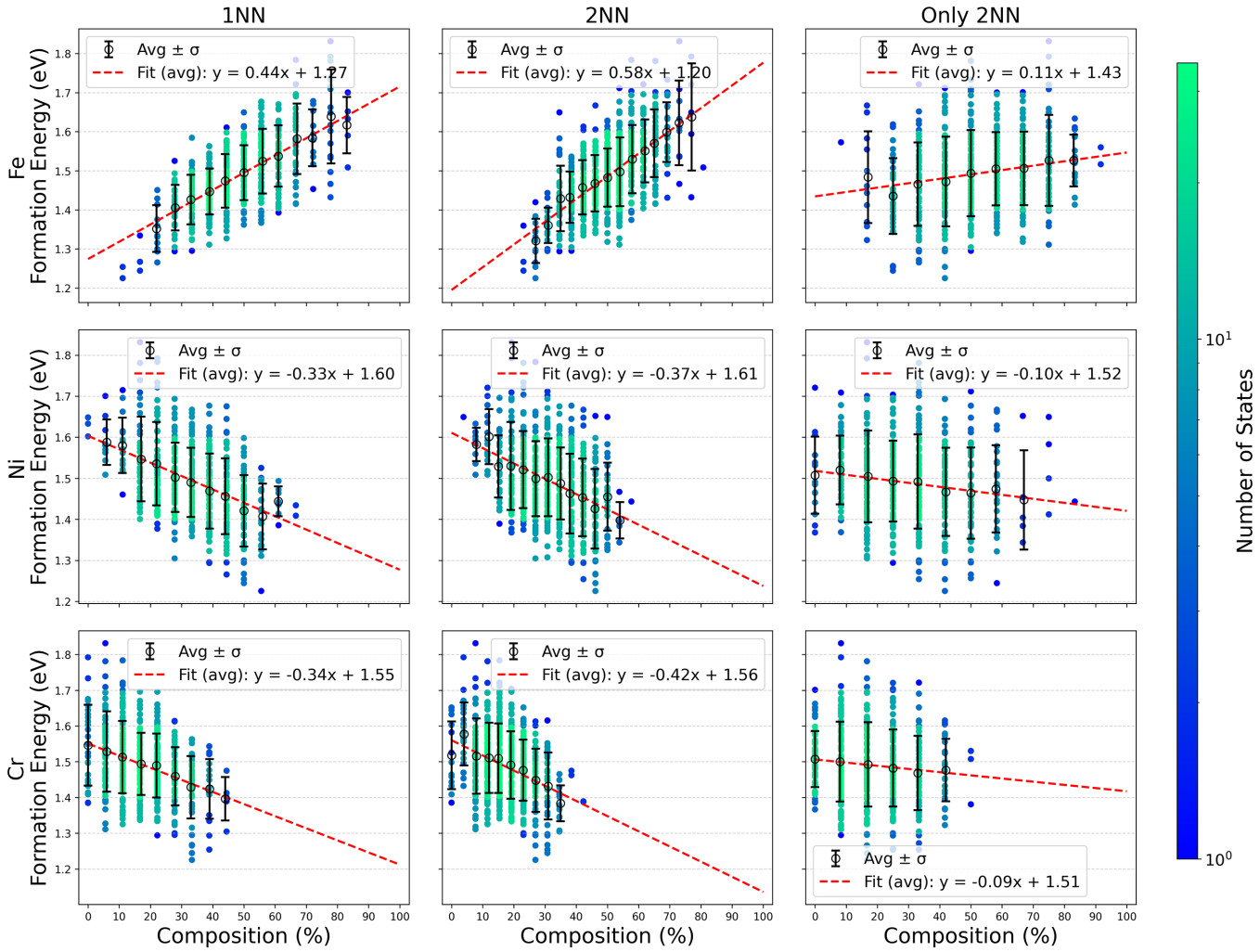

FIG. 4. Correlation between formation energy per vacancy and local atomic composition in 1NN-divacancy configurations (two vacancies in the first-nearest neighbor) of FeNiCr (concentrated solid solutions). Each panel presents the formation energy as a function of elemental composition of Fe (top row), Ni (middle row), and Cr (bottom row). (Left) 1NN: includes atoms in the first-nearest-neighbor shell of the vacancies; (center) 2NN: includes all atoms within the second-nearest-neighbor shell in addition to those that also belong to the 1NN shell; and (right) only-2NN: includes atoms belonging exclusively to the second-nearest-neighbor shell but not the 1NN atoms. The x axis represents the atomic fraction (0–100%) of the specified element within the defined local environment, normalized by the total number of atoms in that shell, while the y axis reports the formation energy per vacancy in eV. Individual points represent distinct migration events. Duplicate events—defined by identical local compositions (rounded to 10^{-2}) and differences smaller than 0.01 in the formation energy (eV). Point colors indicate the number of states within each composition—energy bin using logarithmic normalization (bin widths: 1 at.% in composition and 0.1 eV in energy). Open circles with error bars denote the mean ± one standard deviation for each composition bin containing at least five states. Dashed red lines show linear least-squares fits performed on these binned averages, expressed as $y = \text{slope}\, x + \text{intercept}$, where x is the composition fraction scaled from 0 to 1; the slope is reported in units of eV per composition fraction. These linear fits are provided solely as qualitative indicators of first-order sensitivity of formation energy to local composition; they are not intended as unbiased estimators or free-energy fits, particularly in view of the heteroscedastic nature of the data and the negligible thermodynamic relevance of high-energy configurations at low temperatures.

stable vacancy clusters—rising from 28% in the bulk to as high as 42.3% in certain trivacancy configurations—while Fe and Cr concentrations are at or below their respective bulk levels. These compositional patterns validate previous observations of Ni's stabilizing role and Fe/Cr's relative destabilizing influence [13,35]. Altogether, these results establish that the thermodynamic stability of vacancy clusters in FeNiCr CSAs is governed by a synergy between cluster geometry and local chemical composition. Ni-rich local environments promote energetically favorable clustering by reducing formation energies and enhancing local relaxation, whereas Fe and Cr tend to increase energetic penalties for clustering, particularly in extended configurations. Since Fe is the largest of the three species, we can understand this trend as a way to reduce total strain. The origin of the trends for Cr is less clear but could be linked to its overall tendency to phase separate. These insights are corroborated by both simulation and experimental literature, including studies

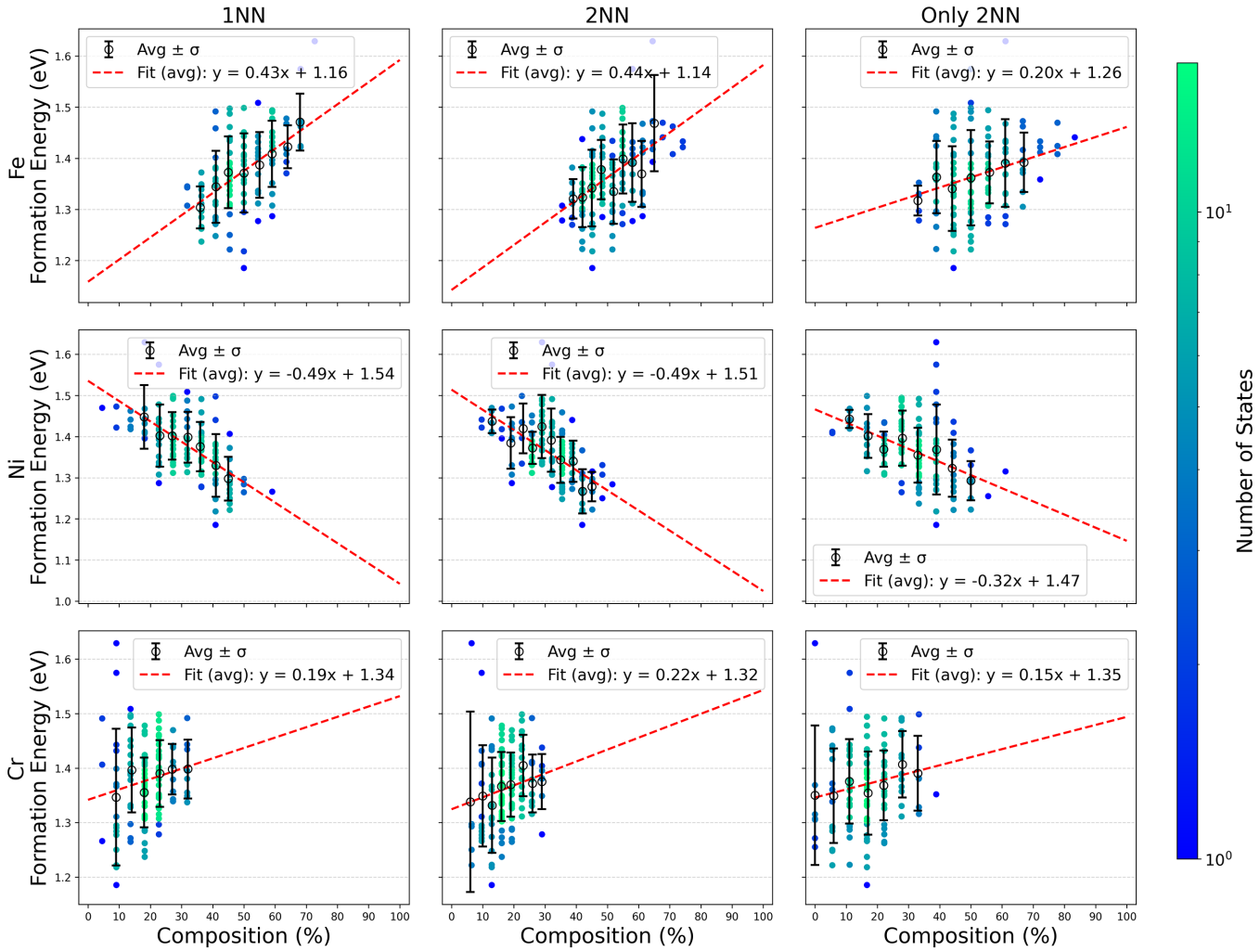

FIG. 5. Correlation between formation energy per vacancy and local atomic composition in 3V(3,0,0,0,0,0) trivacancy configurations (Three 1NN vacancy-pair separations) of FeNiCr (concentrated solid solutions). Each panel presents the formation energy as a function of elemental composition of Fe (top row), Ni (middle row), and Cr (bottom row). (left) 1NN, including atoms in the first-nearest-neighbor shell of the vacancies; (center) 2NN, including all atoms within the second-nearest-neighbor shell, including those that also belong to the 1NN shell; and (right) only-2NN, including atoms belonging exclusively to the second-nearest-neighbor shell and excluding all 1NN atoms. The x axis represents the atomic fraction (0–100%) of the specified element within the defined local environment, normalized by the total number of atoms in that shell, while the y axis reports the formation energy per vacancy in eV. Individual points represent distinct migration events. Duplicate events—defined by identical local compositions (rounded to 10^{-2}) and differences smaller than 0.01 in the formation energy (eV)—were removed. Point colors indicate the number of states within each composition–energy bin using logarithmic normalization (bin widths: 1 at.% in composition and 0.1 eV in energy). Open circles with error bars denote the mean ± one standard deviation for each composition bin containing at least five states. Dashed red lines show linear least-squares fits performed on these binned averages, expressed as $y = \text{slope}\, x + \text{intercept}$, where x is the composition fraction scaled from 0 to 1; the slope is reported in units of eV per composition fraction. These linear fits are provided solely as qualitative indicators of first-order sensitivity of formation energy to local composition; they are not intended as unbiased estimators or free-energy fits, particularly in view of the heteroscedastic nature of the data and the negligible thermodynamic relevance of high-energy configurations at low temperatures.

on positron lifetime evolution, migration enthalpy, and local bonding environment effects in FeCrNi-based austenitic steels [34].

B. Kinetics of vacancy clusters: Energetics, pathways, and entropic effects

We now turn our attention to the analysis of the energy landscape and diffusion characteristics of vacancy clusters in FeNiCr concentrated solid solutions (CSS). Vacancy-mediated diffusion in concentrated solid-solution alloys (CSAs) such as FeNiCr is influenced by a complex interplay between migration energy barriers, available diffusion pathways, and the vibrational entropy captured by the hTST prefactor. These thermally activated processes underpin defect evolution and the radiation response of high-performance structural materials. In this section, we analyze over 295 000 diffusion events involving di-, tri-, and tetravacancy clusters to quantify how migration barriers and hTST prefactors vary

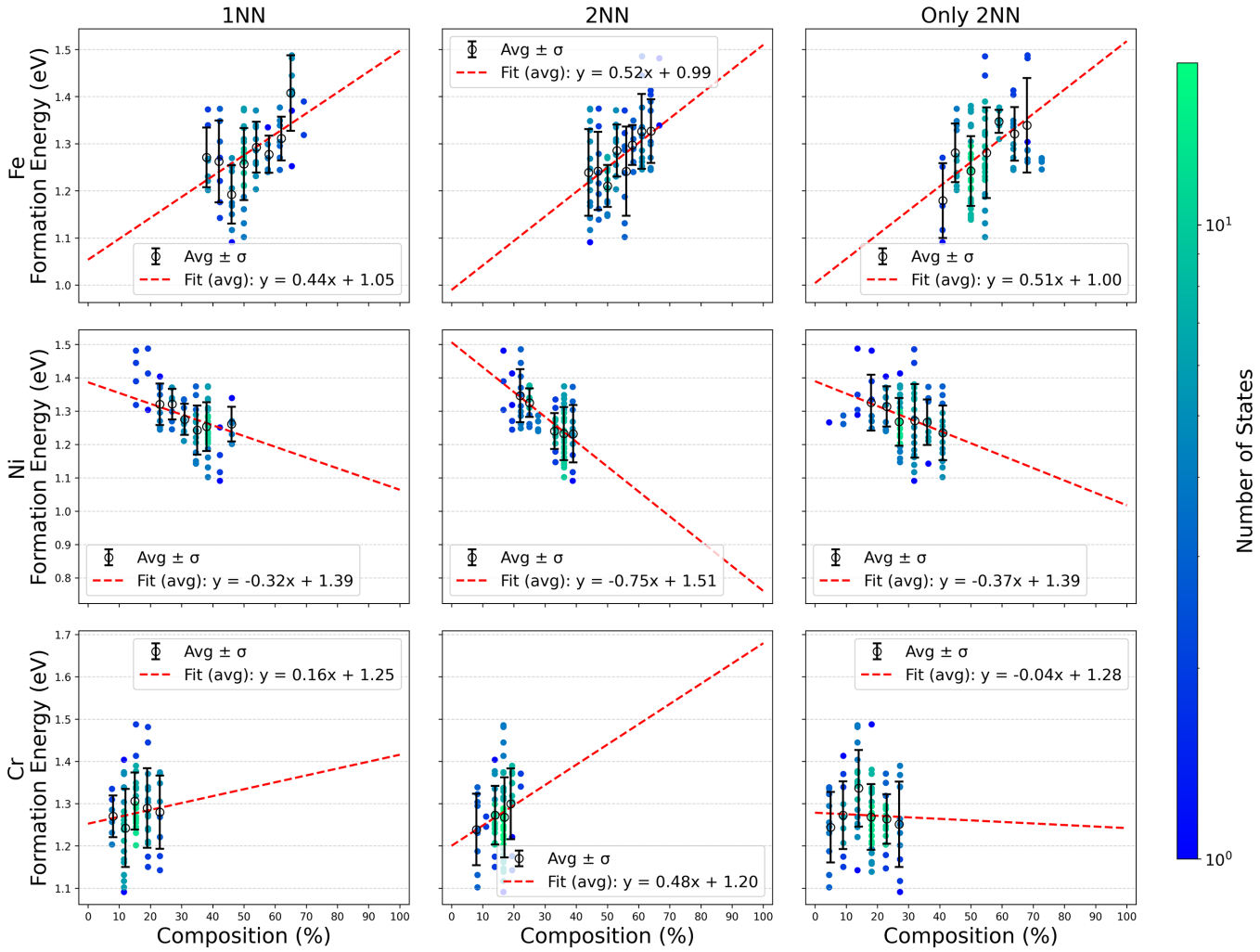

FIG. 6. Correlation between formation energy per vacancy and local atomic composition in 4V(5,1,0,0,0,0) tetravacancy configurations. (Three 5NN vacancy-pair separations and one 1NN vacancy-pair separation) of FeNiCr (concentrated solid solutions.) Each panel presents the formation energy as a function of elemental composition of Fe (top row), Ni (middle row), and Cr (bottom row). (Left) 1NN, including atoms in the first-nearest-neighbor shell of the vacancies; (center) 2NN, including all atoms within the second-nearest-neighbor shell, including those that also belong to the 1NN shell; and (right) only-2NN, including atoms belonging exclusively to the second-nearest-neighbor shell and excluding all 1NN atoms. The x axis represents the atomic fraction (0–100%) of the specified element within the defined local environment, normalized by the total number of atoms in that shell, while the y axis reports the formation energy per vacancy in eV. Individual points represent distinct migration events. Duplicate events—defined by identical local compositions (rounded to 10^{-2}) and differences smaller than 0.01 in the formation energy (eV). Point colors indicate the number of states within each composition–energy bin using logarithmic normalization (bin widths: 1 at.% in composition and 0.1 eV in energy). Open circles with error bars denote the mean ± one standard deviation for each composition bin containing at least five states. Dashed red lines show linear least-squares fits performed on these binned averages, expressed as $y = \text{slope}\, x + \text{intercept}$, where x is the composition fraction scaled from 0 to 1; the slope is reported in units of eV per composition fraction. These linear fits are provided solely as qualitative indicators of first-order sensitivity of formation energy to local composition; they are not intended as unbiased estimators or free-energy fits, particularly in view of the heteroscedastic nature of the data and the negligible thermodynamic relevance of high-energy configurations at low temperatures.

with local composition and configuration, and how they combine to control diffusion rates and kinetic accessibility of various pathways.

Figure 7 illustrates the relationship between hTST prefactors and their associated energy barriers for the sampled events associated with divacancy, trivacancy, and tetravacancy clusters with the marker size denoting the frequency of barrier-prefactor pairs, and red dashed lines indicating linear fits. A clear trend emerges: low energy barriers (∼0.3–0.6 eV) correlate with high prefactors (∼10^{13}–10^{14} s^{-1}), reflecting minimal entropy penalties in compact configurations, while higher barriers (∼0.9–1.2 eV) align with lower prefactors (∼10^{12}–10^{13} s^{-1}), indicating increased entropy costs for extended structures. This barrier–prefactor compensation reflects the interplay between lattice vibrations and local atomic rearrangements during migration. At the same time, substantial scatter is present across all cluster sizes, highlighting the strong sensitivity of both activation barriers and vibrational

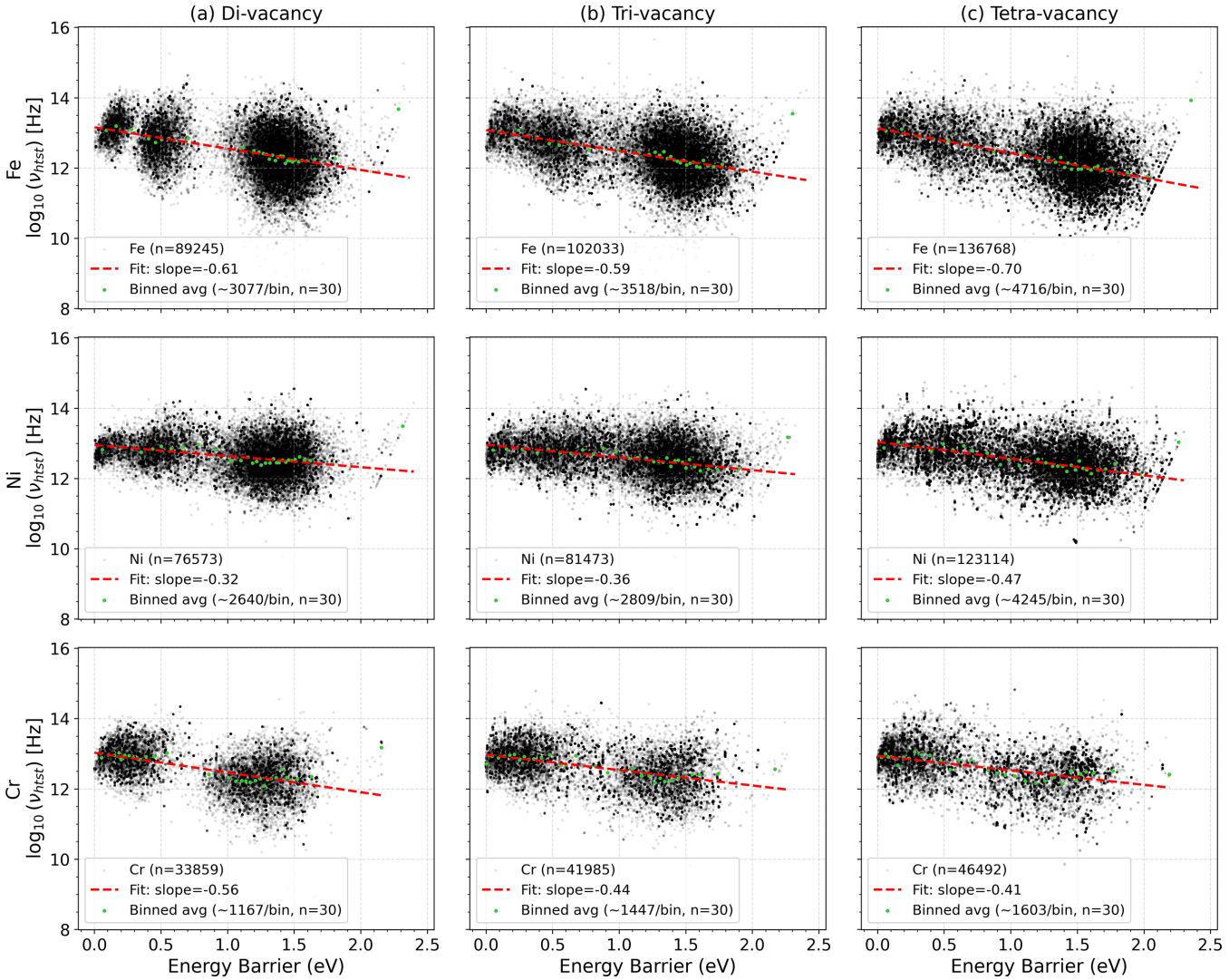

FIG. 7. HTST prefactor analysis showing the relationship between $\log_{10}(\nu_{\text{htst}})$ and energy barriers for vacancy migration in bcc Fe, Ni, and Cr for all generated events (199 677 for divacancy, 225 491 for the trivacancy, and 306 374 for the tetravacancy). The 3×3 grid presents results for (columns left to right) divacancy, trivacancy, and tetravacancy configurations, with (rows top to bottom) iron, nickel, and chromium systems. Black markers represent individual migration events, with marker transparency scaled by the frequency of overlapping data points. Red dashed lines denote least-squares linear fits to the raw data. Green markers show nonuniform, equal-count binned averages of $\log_{10}(\nu_{\text{htst}})$, where bin widths adapt to maintain approximately equal numbers of events per bin. The x axis shows the migration energy barrier (eV), and the y axis shows the logarithm of the HTST attempt frequency (Hz).

entropies to the local chemical environment and the specific atomic pathway involved in each event. Compared to Lefèvre López *et al.* [15], who reported prefactors of $\sim 10^{12}$–10^{13} s^{-1} for single vacancies in FeNiCr, the broader range for clusters underscores the amplified role of multivacancy interactions, a phenomenon less explored in simpler systems like pure metals [36].

Figure 8 illustrates the distributions of migration barriers, hTST prefactors, and transition rates for transitions between the six dominant bound states of a divacancy complex. The corresponding averages of the migration barrier, hTST prefactor, and transition rate are summarized in Table S1 within the Supplemental Material [37]. The 1NN $\rightarrow$ 1NN transition, with a low barrier (0.43 ± 0.11 eV), a high prefactor (1.07×10^{13} s^{-1}), and a robust transition rate (1.35×10^{9} s^{-1}), dominates owing to minimal atomic rearrangement in the FCC lattice. This suggests that divacancy migration is largely governed by short-range diffusion, where vacancies move between compact, stable configurations. However, as vacancy pairs become more distant (e.g., 1NN $\rightarrow$ 4NN), they require crossing higher barriers (0.72 eV) associated with lower prefactors (6.76×10^{12} s^{-1}) and, hence, lower transition rates (8.92×10^{6} s^{-1}, see Table S1 within the Supplemental Material [37]). The combination of elevated barriers and reduced prefactor values reflects the increased complexity of long-range diffusion, which involves larger structural deformations associated with narrower pathways. This explains why the frequency of such events is significantly reduced. These findings imply that divacancy migration in FeNiCr alloys takes place primarily through adjacent jumps, with long-range diffusion mechanisms playing a much smaller role under typical operating conditions.

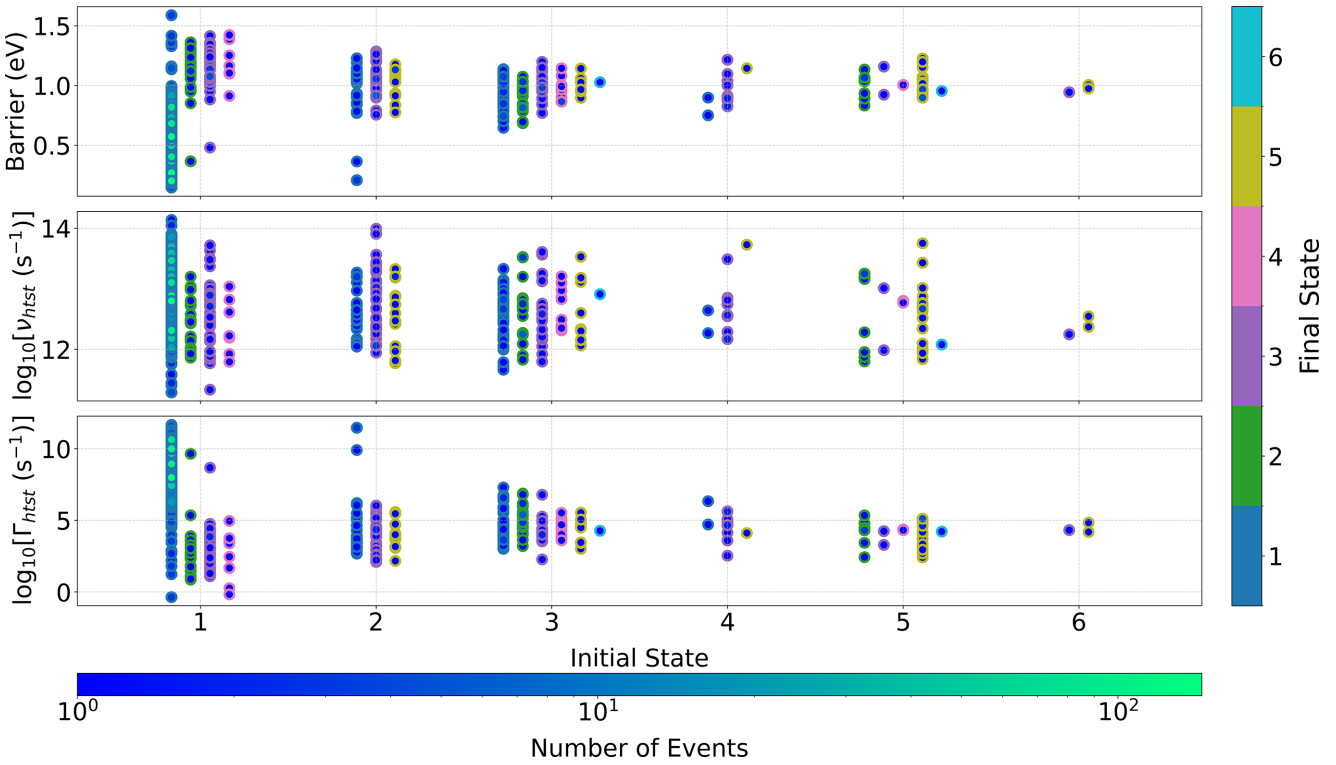

FIG. 8. Scatter plots illustrating (top) migration barriers (eV), (middle) hTST prefactor, and (bottom) transition rate at 600 K for transitions between six dominant bound states of a divacancy complex, plotted against initial state (1–6). For each initial state, data points are horizontally offset by the corresponding final state, using uniform spacing to distinguish individual transition pathways. Marker edge colors encode the final state, while marker face colors represent the number of migration events on a logarithmic scale (winter colormap). Bound states represent vacancy-pair separations: (1) 1NN, (2) 2NN, (3) 3NN, (4) 4NN, (5) 5NN, and (6) 6NN. A horizontal colorbar indicates migration event counts, and a vertical colorbar maps marker edge colors to the final states.

We now turn to the selected mechanisms, associated with the evolution of the system. Figure 9 presents the calculated migration energy barriers, logarithmic harmonic transition state theory (hTST) prefactors, and transition rates for the selected barriers corresponding to the dominant divacancy diffusion mechanism, namely the 1NN $\rightarrow$ 1NN exchange. For this mechanism, Fe, Ni, and Cr exhibit distinct diffusion characteristics. The average migration energy barriers are 0.48 eV for Fe, 0.58 eV for Ni, and 0.32 eV for Cr. The corresponding prefactors are 1.45×10^{13} s^{-1}, 1.21×10^{13} s^{-1}, and 6.17×10^{12} s^{-1}, respectively. Despite Cr exhibiting the lowest barrier, its relatively modest prefactor results in a limited transition rate of 2.7×10^{10} s^{-1}, compared to 2.84×10^{9} s^{-1} for Fe and 4.82×10^{9} s^{-1} for Ni, as shown in Fig. 9(c).

The local chemical environment surrounding the divacancy complex also plays a critical role in modulating diffusion behavior. As detailed in Table I, Ni exhibits a higher-than-bulk concentration in the first-nearest-neighbor (1NN) shell of the divacancy (36% versus a nominal 28%), which likely enhances atomic mobility by locally weakening lattice constraints. In contrast, Cr appears at a lower concentration (17%), indicating a stabilizing effect.

A direct comparison with single-vacancy diffusion data, based on the work of Lefèvre-López *et al.* [15], reveals the significant influence of vacancy clustering on diffusion kinetics. In Fe, the migration energy barrier decreases from 0.84 eV (single vacancy) to 0.48 eV (divacancy), while the prefactor remains constant at 1.5×10^{13} s^{-1}, resulting in a substantial increase in the diffusion rate. Similarly, Ni shows a reduction in barrier from 0.78 eV to 0.58 eV, accompanied by an increase in the prefactor from 8.2×10^{12} s^{-1} to 1.2×10^{13} s^{-1}, thereby enhancing its mobility. Although Cr experiences the most pronounced reduction in energy barrier—from 0.73 eV to 0.32 eV, its prefactor increases only slightly, from 5.3×10^{12} s^{-1} to 6.2×10^{12} s^{-1}.

These observations underscore the importance of both thermodynamic and vibrational factors in governing vacancy-mediated diffusion. While reduced energy barriers in the divacancy configuration generally facilitate increased atomic mobility, the effectiveness of this mechanism depends critically on the accompanying changes in the prefactor. In particular, the limited prefactor enhancement in Cr offsets the impact of the low-energy barrier, highlighting the element-specific nature of diffusion behavior in defect-rich environments. Overall, the low-diffusion barrier for divacancy increases therefore the mobility for the atomic species.

Trivacancy diffusion involves a richer configurational landscape than divacancy diffusion. This increased complexity arises from the greater number of possible bound states, which leads to a larger number of pathways between those states. Figure 10 shows the most frequent and energetically favorable transitions between these configurations, with the

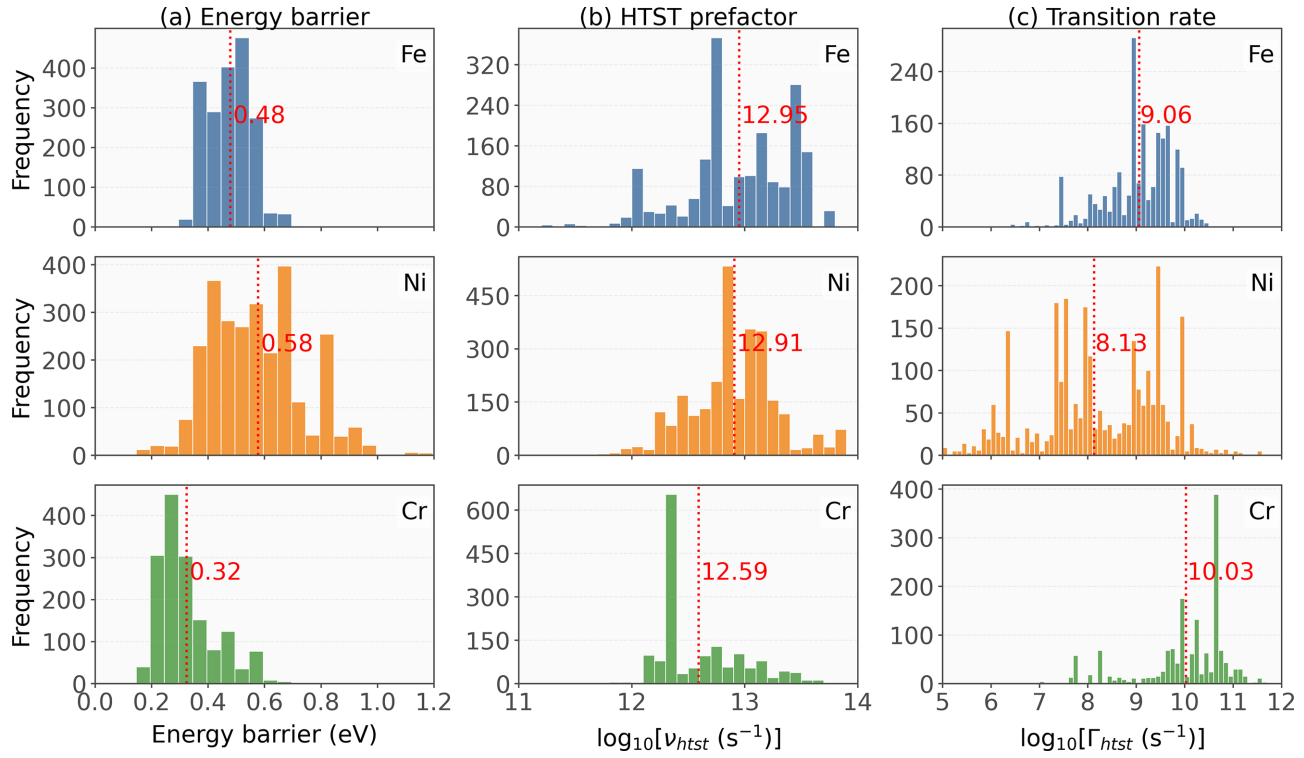

FIG. 9. (a) Distributions of selected energy barriers, (b) diffusion prefactor, and (c) logarithmic values of transition rate at 600 K for the divacancy complex's dominant diffusion mechanism (1NN $\longrightarrow$ 1NN). The average barriers are 0.48 eV, 0.58 eV, and 0.32 eV; average prefactors are 1.45×10^{13} s^{-1}, 1.21×10^{13} s^{-1}, and 6.17×10^{12} s^{-1}; average transition rates are 2.84×10^{9} s^{-1}, 4.82×10^{9} s^{-1}, and 2.72×10^{10} s^{-1} for Fe, Ni, and Cr movement, respectively.

corresponding average migration barriers, hTST prefactors, and transition rates summarized in Table S2 within the Supplemental Material [37]. The most kinetically favorable transition identified is the self-transition within the 3V(3,0,0,0,0,0) state. This involves a local rearrangement or exchange of atoms that preserves the overall configuration class but may slightly rotate or reorient the trivacancy cluster without altering its spatial footprint. Despite being a "no-change" event in topological terms, this transition is kinetically relevant. It proceeds with a migration barrier of 0.44 ± 0.17 eV, a prefactor of 1.09×10^{13} s^{-1}, and a rate of 5.59×10^{9} s^{-1}. These transitions are important for enabling configurational entropy within bound clusters and facilitating subsequent directional migration.

Another frequently occurring process is the transition from 3V(3,0,0,0,0,0) to 3V(2,1,0,0,0,0). This event involves the reconfiguration of a trivacancy cluster with three 1NN vacancy pairs into one with two 1NN and one 2NN pairs, effectively introducing a small spatial dilatation while maintaining cluster compactness. The transition exhibits a low migration barrier of 0.51 ± 0.104 eV, coupled with a high hTST prefactor of 8.57×10^{12} s^{-1}. These parameters yield a transition rate of 1.19×10^{9} s^{-1}, making it one of the most frequent and energetically accessible trivacancy events. The reverse transition, 3V(2,1,0,0,0,0) $\rightarrow$ 3V(3,0,0,0,0,0), proceeds through a similar atomic mechanism and exhibits comparable energetics, with a slightly lower barrier of 0.35 eV and a transition rate of 1.24×10^{10} s^{-1}, indicating a dynamically reversible pair of configurations that can exchange rapidly at moderate temperatures.

In contrast, transitions toward more extended configurations are characterized by significantly higher energetic and entropic penalties. For example, the migration from 3V(3,0,0,0,0,0) $\rightarrow$ 3V(1,0,1,0,1,0) results in a less compact cluster geometry involving 1NN, 3NN, and 5NN separations. This transition exhibits a higher barrier of 0.60 ± 0.09 eV, a prefactor of 7.52×10^{12} s^{-1}, and a transition rate of only 1.33×10^{8} s^{-1}. The steep drop in rate, by more than two orders of magnitude compared to compact transitions, demonstrates again that extended configurations are kinetically suppressed under thermal conditions typical of diffusion-driven microstructural evolution.

Figures 11 and 12 highlight the role of atomic species—Fe, Ni, and Cr—in mediating trivacancy migration events, whereas Figs. S1–S3 within the Supplemental Material [37] illustrate alternative migration mechanisms. One of the most frequent and illustrative transitions is 3V(3,0,0,0,0,0) $\rightarrow$ 3V(3,0,0,0,0,0), a localized rearrangement within a tightly bound trivacancy configuration. As shown in Fig. 11(a), as for the other defects, the migration barrier for Cr (0.37 eV) is significantly lower than that for the two other elements (0.47 eV for Fe, 0.45 eV for Ni). These differences arise from the distinct local stiffness and bonding strength of each species. Cr, having the lowest barrier, provides a comparatively open and energetically favorable migration pathway, despite its generally stiffer vibrational character in extended configurations.

The associated hTST prefactors, shown in Fig. 11(b), are likewise species-dependent. Fe, Ni, and Cr exhibit average prefactors of 1.34×10^{13} s^{-1}, 1.07×10^{13} s^{-1}, and

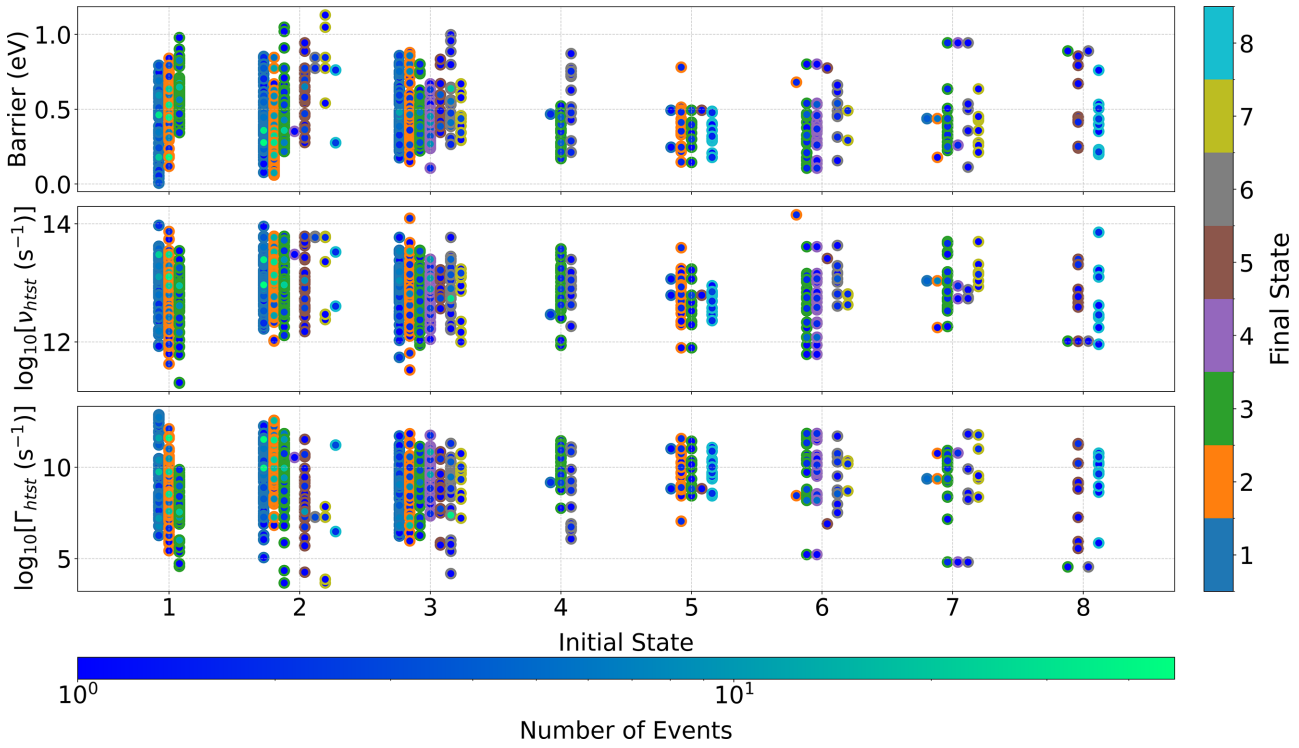

FIG. 10. Scatter plots illustrating (top) migration barriers (eV), (middle) hTST prefactor, and (bottom) transition rate at 600 K for transitions between eight dominant bound states of a trivacancy complex, plotted against initial state (1–8). For each initial state, data points are horizontally offset by the corresponding final state, using uniform spacing to distinguish individual transition pathways. Marker edge colors encode the final state, while marker face colors represent the number of migration events on a logarithmic scale (winter colormap). Bound states represent vacancy-pair separations: (1) 3V(3,0,0,0,0,0): three 1NN vacancy-pair separations; (2) 3V(2,1,0,0,0,0): two 1NN, and one 2NN vacancy-pair separations; (3) 3V(2,0,1,0,0,0): two 1NN, and one 3NN vacancy-pair separations; (4) 3V(2,0,0,1,0,0): two 1NN and one 4NN vacancy-pair separations; (5) 3V(1,1,1,0,0,0): one 1NN, one 2NN, and one 3NN vacancy-pair separations; (6) 3V(1,0,1,1,0,0): one 1NN, one 3NN and one 4NN vacancy-pair separations; (7) 3V(1,0,2,0,0,0): one 1NN, and two 3NN vacancy-pair separations; and (8) 3V(1,1,0,0,1,0): one 1NN, one 2NN, and one 5NN vacancy-pair separations. A horizontal colorbar indicates migration event counts, and a vertical colorbar maps marker edge colors to the final states. Events with higher multiplicity are plotted on top, highlighting kinetically dominant migration pathways.

1.66×10^{13} s^{-1}, respectively. These values reflect the local vibrational environments at the saddle point: Fe and Cr transitions typically involve less structural deformation and smaller entropy penalties, whereas Ni, with its more flexible bonding, allows for greater vibrational mode variation, reducing the prefactor despite comparable or higher energy barriers.

The combined effect of the barrier and the prefactor is captured in the transition rate distributions in Fig. 11(c). Interestingly, the compensation between the prefactor and the barrier yields transition rates of 2.63×10^{9} s^{-1} for Fe, 2.51×10^{9} s^{-1} for Ni, and 1.34×10^{10} s^{-1} for Cr. Despite variations in bonding strength and stiffness, all three species can therefore effectively mediate fast trivacancy migration, provided the configuration is compact and the saddle-point geometry is favorable.

Another key transition analyzed in species-resolved detail is 3V(3,0,0,0,0,0) → 3V(2,1,0,0,0,0) (Fig. 12). The migration barrier is 0.55 eV for Fe, 0.53 eV for Ni, and 0.32 eV for Cr [Fig. 12(a)]. Prefactors remain in the $10^{12} - 10^{13}$ s^{-1} range for all three species, with Fe at 8.32×10^{12} s^{-1}, Ni at 5.62×10^{12} s^{-1}, and Cr at 1.26×10^{13} s^{-1} [Fig. 12(b)].

The transition rates for this pathway, presented in Fig. 12(c), reflect the enhanced kinetics of this particular rearrangement. Cr shows a rate of 2.51×10^{10} s^{-1}, followed by Ni (2.00×10^{8} s^{-1}) and Fe (1.91×10^{8} s^{-1}). With rates two orders of magnitude faster than Fe and Ni, the Cr-mediated pathway stands, highlighting the dominant role of compact geometry and local chemical effects in governing trivacancy dynamics.

Overall, although Ni tends to exhibit slightly higher energy barriers and lower prefactors than Fe or Cr, it still contributes significantly to trivacancy migration owing to its abundance and favorable bonding environment in FCC alloys. Cr, often associated with reduced monovacancy mobility because of stiffer bonds, appears to facilitate fast migration in compact trivacancy geometries, which is likely because of a favorable arrangement of saddle-point forces and minimal disruption of its electronic structure.

Figure 13 depicts the most frequent and energetically favorable transitions between these configurations, with the corresponding average migration barriers, hTST prefactors, and transition rates for transitions between the nine dominant bound states of a tetravacancy complex summarized in Table

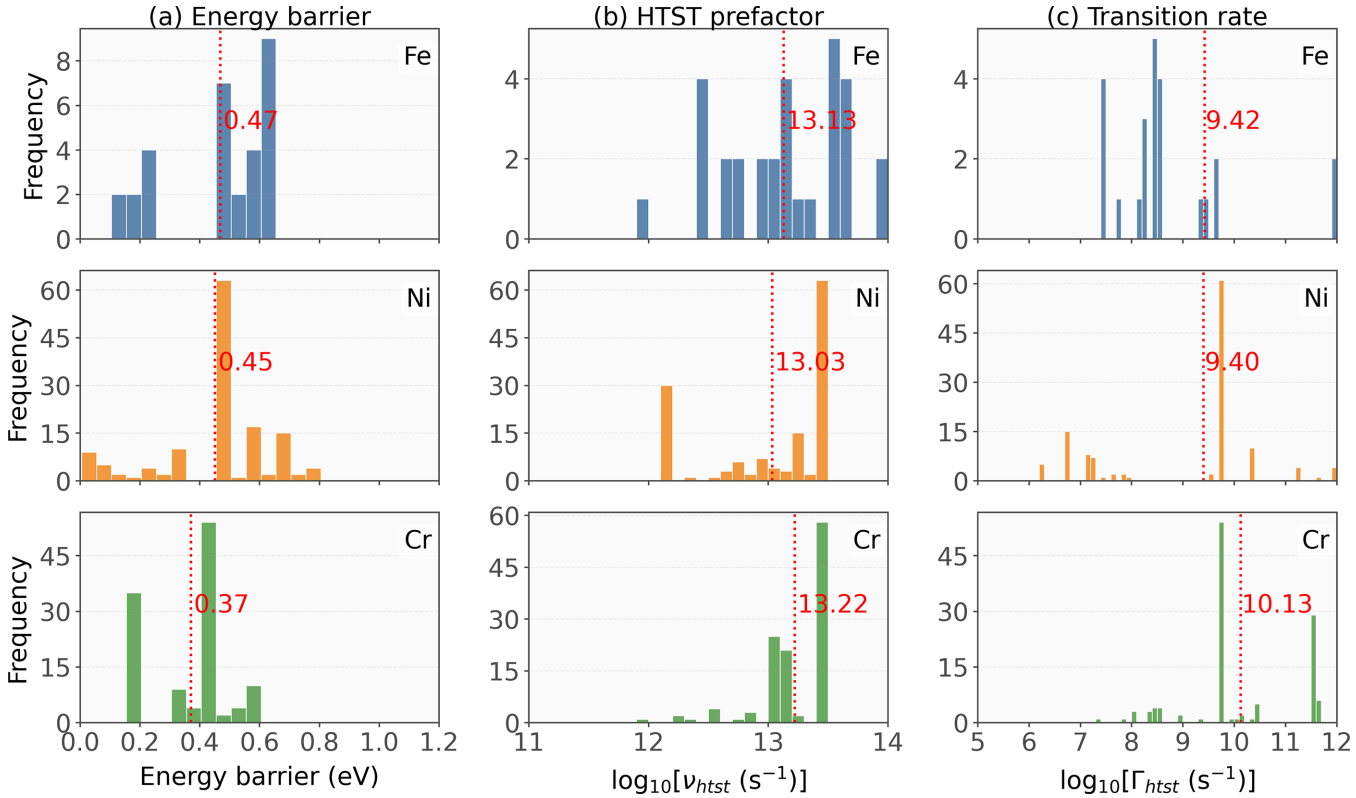

FIG. 11. Distributions of (a) selected energy barriers, (b) hTST prefactors, and (c) transition rate at 600 K for the trivacancy diffusion mechanism [3V(3,0,0,0,0,0) → 3V(3,0,0,0,0,0)]. The average barriers are 0.47 eV, 0.45 eV, and 0.37 eV; the average prefactors are 1.34×10^{13} s^{-1}, 1.07×10^{13} s^{-1}, and 1.66×10^{13} s^{-1}; the average hTST transition rates are 2.63×10^{9} s^{-1}, 2.51×10^{9} s^{-1}, and 1.34×10^{10} s^{-1} for Fe, Ni, and Cr movement, respectively.

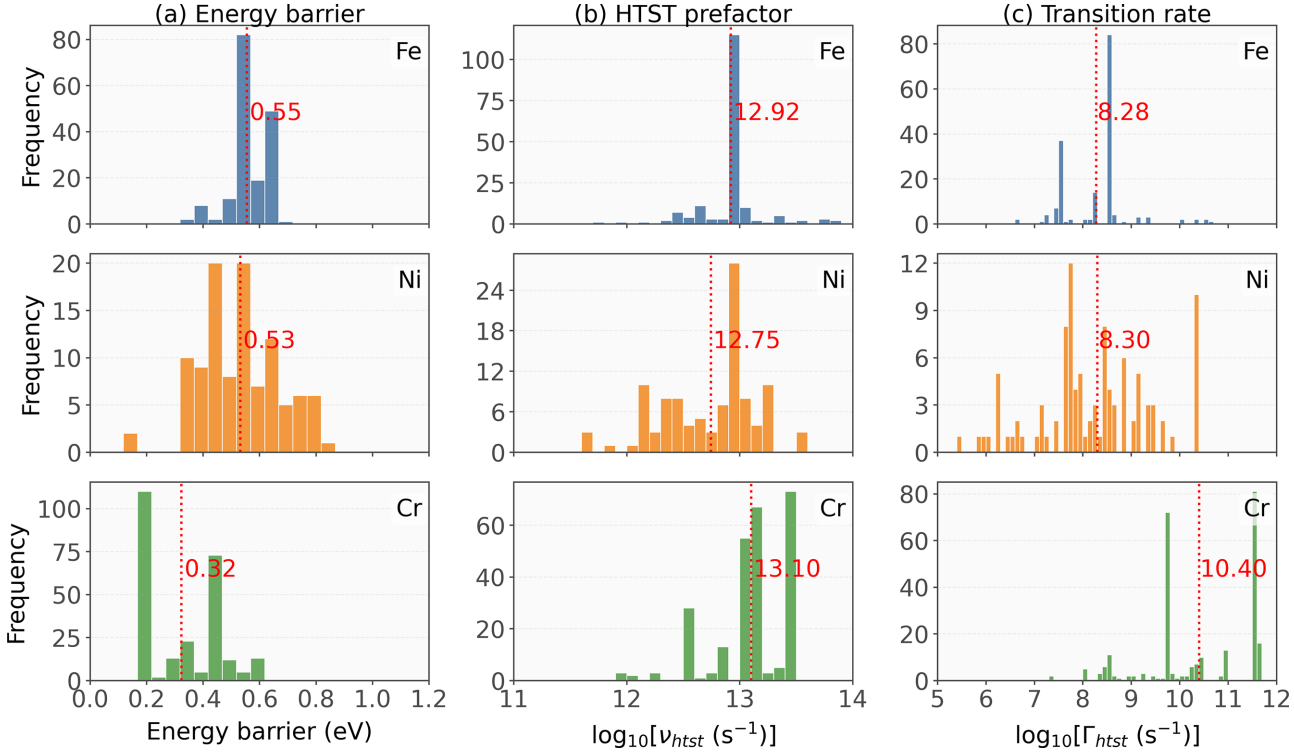

FIG. 12. Distributions of (a) selected energy barriers, (b) hTST prefactors, and (c) transition rate at 600 K for the dominant trivacancy diffusion mechanism [3V(3,0,0,0,0,0) → 3V(2,1,0,0,0,0)]. The average barriers are 0.55 eV, 0.53 eV, and 0.32 eV; average prefactors are 8.32×10^{12} s^{-1}, 5.62×10^{12} s^{-1}, and 1.26×10^{13} s^{-1}; average hTST transition rates are 1.91×10^{8} s^{-1}, 2.00×10^{8} s^{-1}, and 2.51×10^{10} s^{-1} for Fe, Ni, and Cr movement, respectively.

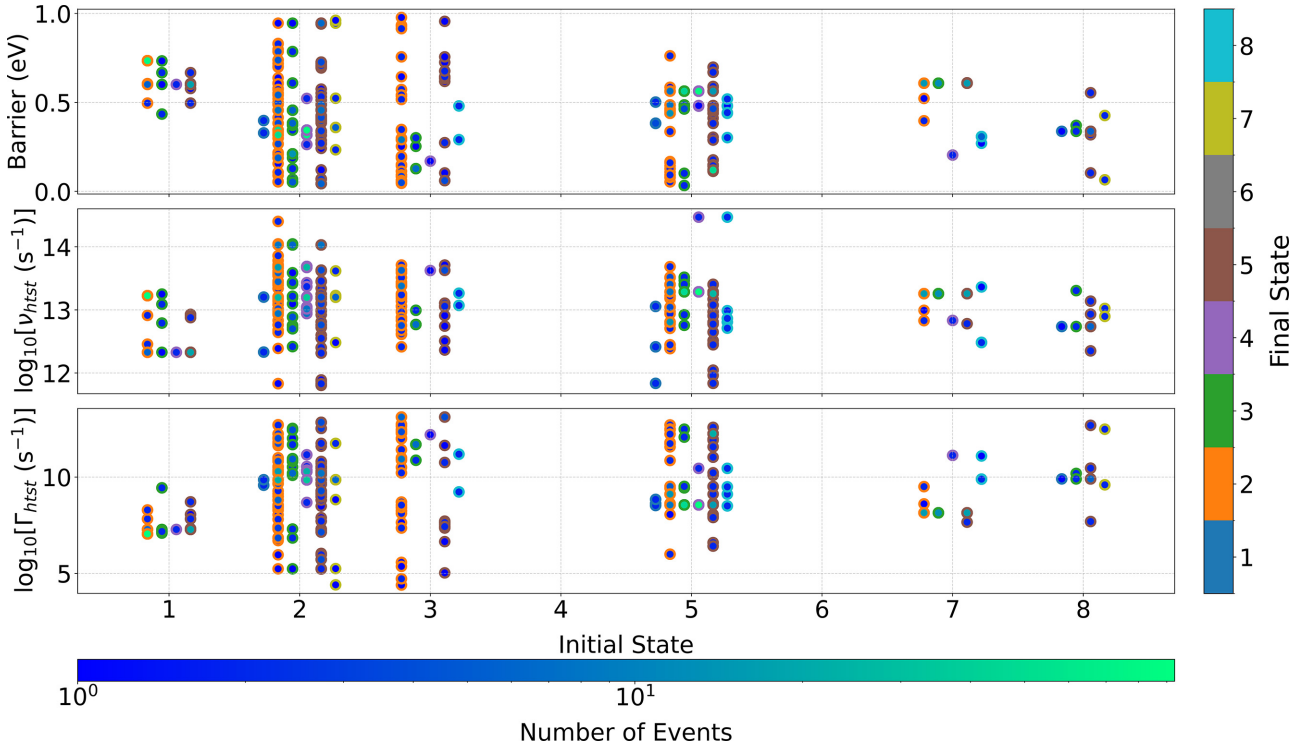

FIG. 13. Scatter plots illustrating (top) migration barriers (eV), (middle) hTST prefactor, and (bottom) transition rate at 600 K for transitions between eight dominant bound states of a tetravacancy complex, plotted against initial state (1–8). For each initial state, data points are horizontally offset by the corresponding final state, using uniform spacing to distinguish individual transition pathways. Marker edge colors encode the final state, while marker face colors represent the number of migration events on a logarithmic scale (winter colormap). Bound states represent vacancy-pair separations: (1) 4V(6,0,0,0,0,0): six 1NN vacancy-pair separations; (2) 4V(5,1,0,0,0,0): five 1NN and one 2NN vacancy-pair separations; (3) 4V(5,0,1,0,0,0): five 1NN and one 3NN vacancy-pair separations; (4) 4V(4,2,0,0,0,0): four 1NN and two 2NN vacancy-pair separations; (5) 4V(4,1,1,0,0,0): four 1NN, one 2NN, and one 3NN vacancy-pair separations; (6) 4V(2,2,0,0,2,0): two 1NN, two 2NN, and two 5NN vacancy-pair separations; (7) 4V(4,0,2,0,0,0): four 1NN and two 3NN vacancy-pair separations; and (8) 4V(4,0,1,1,0,0): four 1NN, one 3NN, and one 4NN vacancy-pair separations. A horizontal colorbar indicates migration event counts, and a vertical colorbar maps marker edge colors to the final states. Events with higher multiplicity are plotted on top, highlighting kinetically dominant migration pathways.

S3 within the Supplemental Material [37]. The most kinetically favorable transition identified is the self-transition within the bound state of 4V(5,1,0,0,0,0) having a migration barrier of 0.35 eV, a prefactor of 2.1×10^{13} s^{-1}, and a transition rate of 2.35×10^{10} s^{-1}. These pathways involve short-range atomic movements within compact configurations, similar to those observed in di- and trivacancy complexes. This efficient short-range diffusion is crucial for maintaining localized defect mobility, thereby reducing the likelihood of significant material degradation. Figure 14 illustrates the role of atomic species, Fe, Ni, and Cr, in mediating migration events 4V(5,1,0,0,0,0) → 4V(5,1,0,0,0,0). The transition exhibits average barriers of 0.46 eV (Fe), 0.39 eV (Ni), and 0.34 eV (Cr), with corresponding prefactors of 2.34×10^{13} s^{-1}, 2.69×10^{13} s^{-1}, and 3.02×10^{13} s^{-1} [Figs. 14(a) and 14(b)]. These values yield transition rates of 4.47×10^{9} s^{-1} (Fe), 6.46×10^{9} s^{-1} (Ni), and 4.27×10^{10} s^{-1} (Cr) [Fig. 14(c)], highlighting Cr as the fastest mediator because of its combination of low barrier and high prefactor.

The 4V(5,1,0,0,0,0) → 4V(5,0,1,0,0,0) transition, shown in Fig. 15, has average barriers of 0.49 eV (Fe), 0.32 eV (Ni), and 0.28 eV (Cr). The associated prefactors are 6.61×10^{12} s^{-1}, 2.34×10^{13} s^{-1}, and 1.35×10^{13} s^{-1}, leading to transition rates of 5.01×10^{8} s^{-1} (Fe), 5.01×10^{10} s^{-1} (Ni), and 5.75×10^{10} s^{-1} (Cr). These results confirm that Ni and Cr enable much faster migration pathways than Fe.

Overall, across all cluster sizes, Cr-mediated transitions consistently exhibit lower selective migration barriers and higher transition rates than Fe- or Ni-mediated transitions, indicating that Cr atoms participate most frequently in vacancy-cluster migration events. Iron-mediated transitions show intermediate behavior, whereas Ni-mediated transitions are comparatively suppressed because of higher barriers. These results characterize event-level mediation within vacancy-cluster diffusion mechanisms rather than macroscopic tracer diffusion; nevertheless, they demonstrate that local chemical identity plays a critical role in controlling the kinetics of vacancy-cluster migration in FeNiCr concentrated solid solutions.

C. Influence of local chemical environment on vacancy cluster migration

The influence of local chemical composition on vacancy-cluster migration in FeNiCr concentrated solid solutions was examined by correlating migration barriers, hTST prefactors,

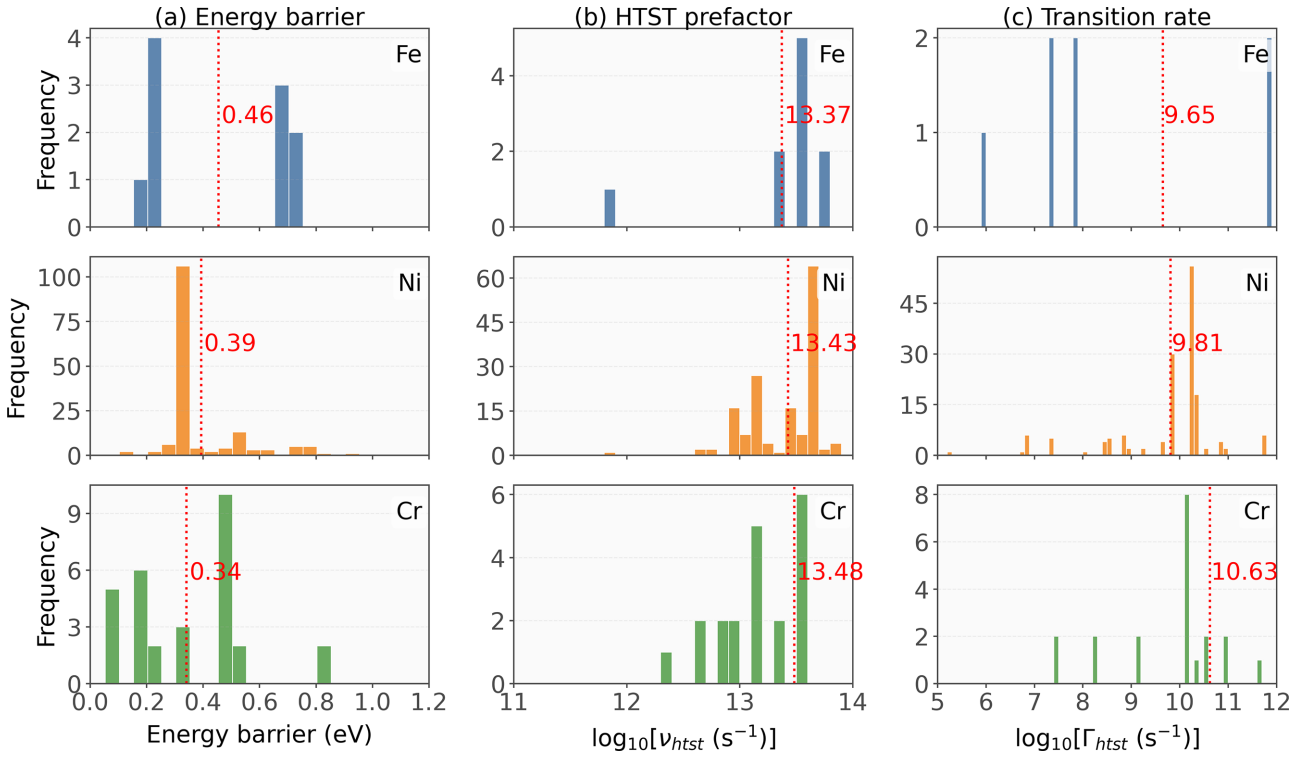

FIG. 14. Distributions of (a) selected energy barriers, (b) hTST prefactors, and (c) transition rate at 600 K for the dominant tetravacancy diffusion mechanism [4V(5,1,0,0,0,0) → 4V(5,1,0,0,0,0)]. The average barriers are 0.46 eV, 0.39 eV, and 0.34 eV; average prefactors are 2.34×10^{13} s^{-1}, 2.69×10^{13} s^{-1}, and 3.02×10^{13} s^{-1}; average hTST transition rates are 4.47×10^{9} s^{-1}, 6.46×10^{9} s^{-1}, and 4.27×10^{10} s^{-1} for Fe, Ni, and Cr movement, respectively.

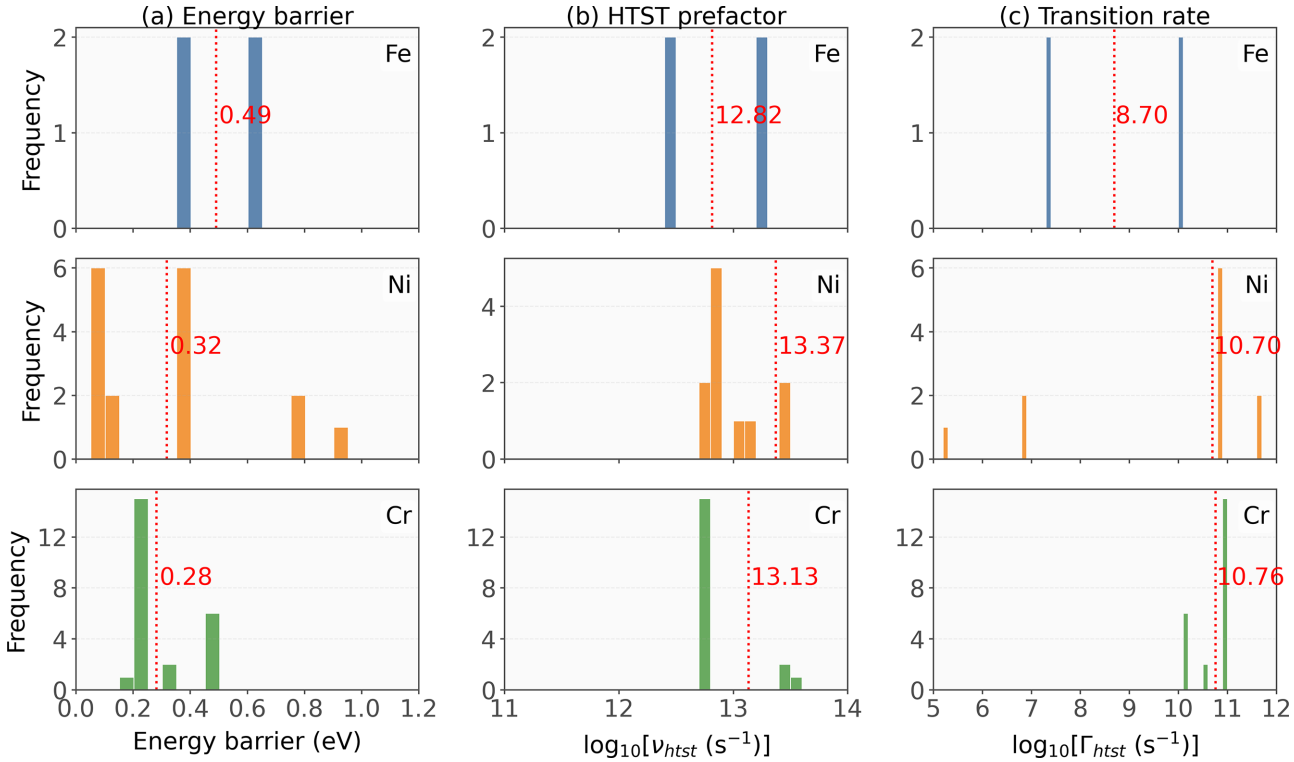

FIG. 15. Distributions of (a) selected energy barriers, (b) hTST prefactors, and (c) transition rate at 600 K for the dominant tetravacancy diffusion mechanism [4V(5,1,0,0,0,0) → 4V(5,0,1,0,0,0)]. The average barriers are 0.49 eV, 0.32 eV, and 0.28 eV; average prefactors are 6.61×10^{12} s^{-1}, 2.34×10^{13} s^{-1}, and 1.35×10^{13} s^{-1}; average hTST transition rates are 5.01×10^{8} s^{-1}, 5.01×10^{10} s^{-1}, and 5.75×10^{10} s^{-1} for Fe, Ni, and Cr movement, respectively.

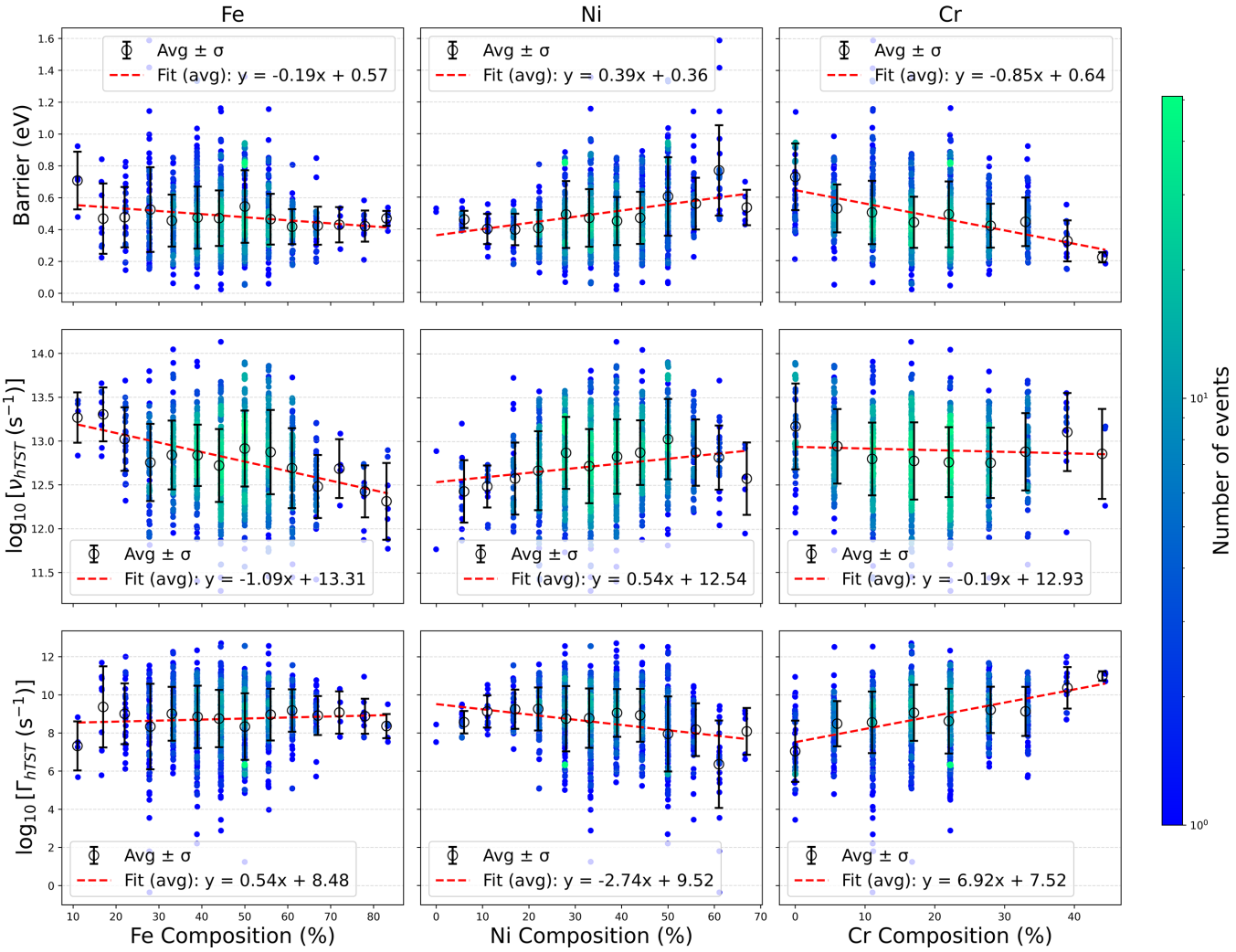

FIG. 16. Relationship between vacancy cluster migration properties and local first-nearest-neighbor (1NN) compositions during divacancy cluster migration (1NN → 1NN). The rows correspond to: (top) migration barrier energy (eV), (middle) logarithm of the hTST prefactor ($\log_{10}[\nu_{\mathrm{hTST}}\ \mathrm{s}^{-1}]$), and (bottom) logarithm of the hTST rate ($\log_{10}[\Gamma_{\mathrm{hTST}}\ \mathrm{s}^{-1}]$) at 600 K. Columns correspond to the elemental composition fractions of Fe, Ni, and Cr in the initial-state 1NN shell surrounding the migrating cluster. The x axis shows the atomic percentage of each element in the specified environment (0–100%), and the y axis corresponds to the migration property. Individual points represent distinct migration events. Duplicate events—defined by identical local compositions (rounded to 10^{-2}) and differences smaller than 0.01 in the migration barrier (eV), $\log_{10}\nu_{\mathrm{hTST}}$, and $\log_{10}\Gamma_{\mathrm{hTST}}$—were removed. Point colors indicate the number of events in each composition–property bin using logarithmic normalization (bin widths: 1 at.% in composition; 0.02 eV for barriers; 0.10 for $\log_{10}\nu_{\mathrm{hTST}}$ and $\log_{10}\Gamma_{\mathrm{hTST}}$). Open gray circle with error bars denote the mean ± one standard deviation for each composition bin containing at least three events. Dashed red lines show linear least-squares fits performed on the binned averages, expressed as $y = \mathrm{slope} \times x + \mathrm{intercept}$, where x is the composition scaled from 0 to 1, and the slope units correspond to the property: eV per fraction for migration barriers, $\log_{10}(\mathrm{s}^{-1})$ per fraction for hTST prefactors, and $\log_{10}(\mathrm{s}^{-1})$ per fraction for hTST rates.

and transition rates with the elemental concentrations in the first-nearest-neighbor (1NN) shell of the initial state surrounding the migrating cluster, as summarized in Figs. 16–20 for representative di-, tri-, and tetravacancy mechanisms. Across all cluster sizes, migration kinetics exhibit a barrier-dominated dependence on the initial-state local composition: Increasing the Ni concentration consistently raises migration barriers, increasing the Cr concentration lowers them, and Fe produces an intermediate response. Although hTST prefactors provide partial and mechanism-dependent compensation, migration rates are governed primarily by variations in activation barriers.

Figure 16 shows that divacancy migration displays a clear dependence on the local 1NN chemical environment. Increasing the Fe concentration produces a slight reduction in the migration barrier accompanied by a concurrent decrease in the hTST prefactor. These opposing trends largely offset one another, resulting in only a modest net change in the transition rate. In contrast, increasing the Ni concentration leads to a pronounced increase in the migration barrier that dominates the kinetic response and results in strong suppression of migration. Increasing the Cr concentration has the opposite effect, substantially lowering the migration barrier; although the prefactor decreases, the barrier reduction

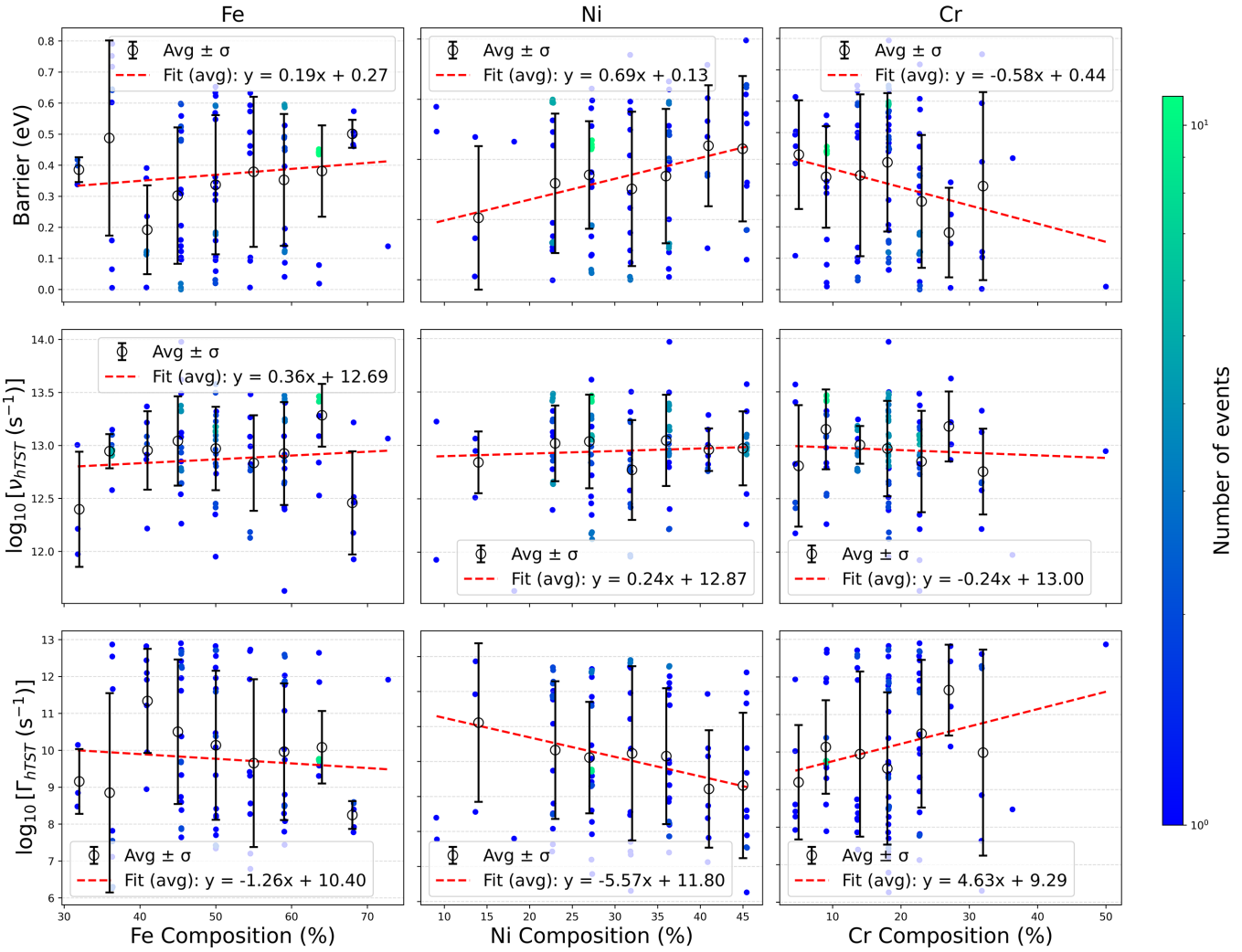

FIG. 17. Correlation between vacancy cluster migration properties and local first-nearest-neighbor (1NN) atomic compositions during 3V(3,0,0,0,0,0) → 3V(3,0,0,0,0,0) migration of a trivacancy cluster. The rows correspond to: (top) migration barrier energy (eV), (middle) logarithm of the hTST prefactor ($\log_{10}[\nu_{\mathrm{hTST}}\ \mathrm{s}^{-1}]$), and (bottom) logarithm of the hTST rate ($\log_{10}[\Gamma_{\mathrm{hTST}}\ \mathrm{s}^{-1}]$) at 600 K. Columns correspond to the elemental composition fractions of Fe, Ni, and Cr in the initial-state 1NN shell surrounding the migrating cluster. The x axis shows the atomic percentage of each element in the specified environment (0–100%), and the y axis corresponds to the migration property. Individual points represent distinct migration events. Duplicate events—defined by identical local compositions (rounded to 10^{-2}) and differences smaller than 0.01 in the migration barrier (eV), $\log_{10}\nu_{\mathrm{hTST}}$, and $\log_{10}\Gamma_{\mathrm{hTST}}$—were removed. Point colors indicate the number of events in each composition–property bin using logarithmic normalization (bin widths: 1 at.% in composition; 0.02 eV for barriers; 0.10 for $\log_{10}\nu_{\mathrm{hTST}}$ and $\log_{10}\Gamma_{\mathrm{hTST}}$). Open gray circle with error bars denote the mean ± one standard deviation for each composition bin containing at least three events. Dashed red lines show linear least-squares fits performed on the binned averages, expressed as $y = \mathrm{slope} \times x + \mathrm{intercept}$, where x is the composition scaled from 0 to 1, and the slope units correspond to the property: eV per fraction for migration barriers, $\log_{10}(\mathrm{s}^{-1})$ per fraction for hTST prefactors, and $\log_{10}(\mathrm{s}^{-1})$ per fraction for hTST rates.

dominates, yielding a marked enhancement of the transition rate. Linear fits to the binned averages in Fig. 16 quantify these trends, with barrier slopes of -0.19 eV/x (Fe), $+0.39$ eV/x (Ni), and -0.85 eV/x(Cr), where x denotes the elemental fraction in the 1NN shell. The corresponding prefactor slopes (-1.09, $+0.54$, and -0.19 $\log_{10}\nu/x$ lead to net rate slopes of $+0.54$, -2.74, and $+6.92$ $\log_{10}\Gamma/x$, respectively.

Figures 17–19 demonstrate that trivacancy migration exhibits a similarly systematic dependence on local 1NN composition across both symmetric and asymmetric migration mechanisms. As in the divacancy case, migration kinetics remain predominantly barrier controlled, with prefactor variations providing secondary, mechanism-dependent modulation. Increasing Ni concentration consistently raises activation barriers and suppresses transition rates across the mechanisms examined; in some pathways this suppression is further reinforced by a concurrent decrease in the hTST prefactor, such that energetic and entropic contributions act cooperatively to reduce trivacancy mobility. Increasing the Cr concentration consistently promotes trivacancy migration through barrier reduction. The associated prefactor response depends on the migration pathway, either partially compensating the

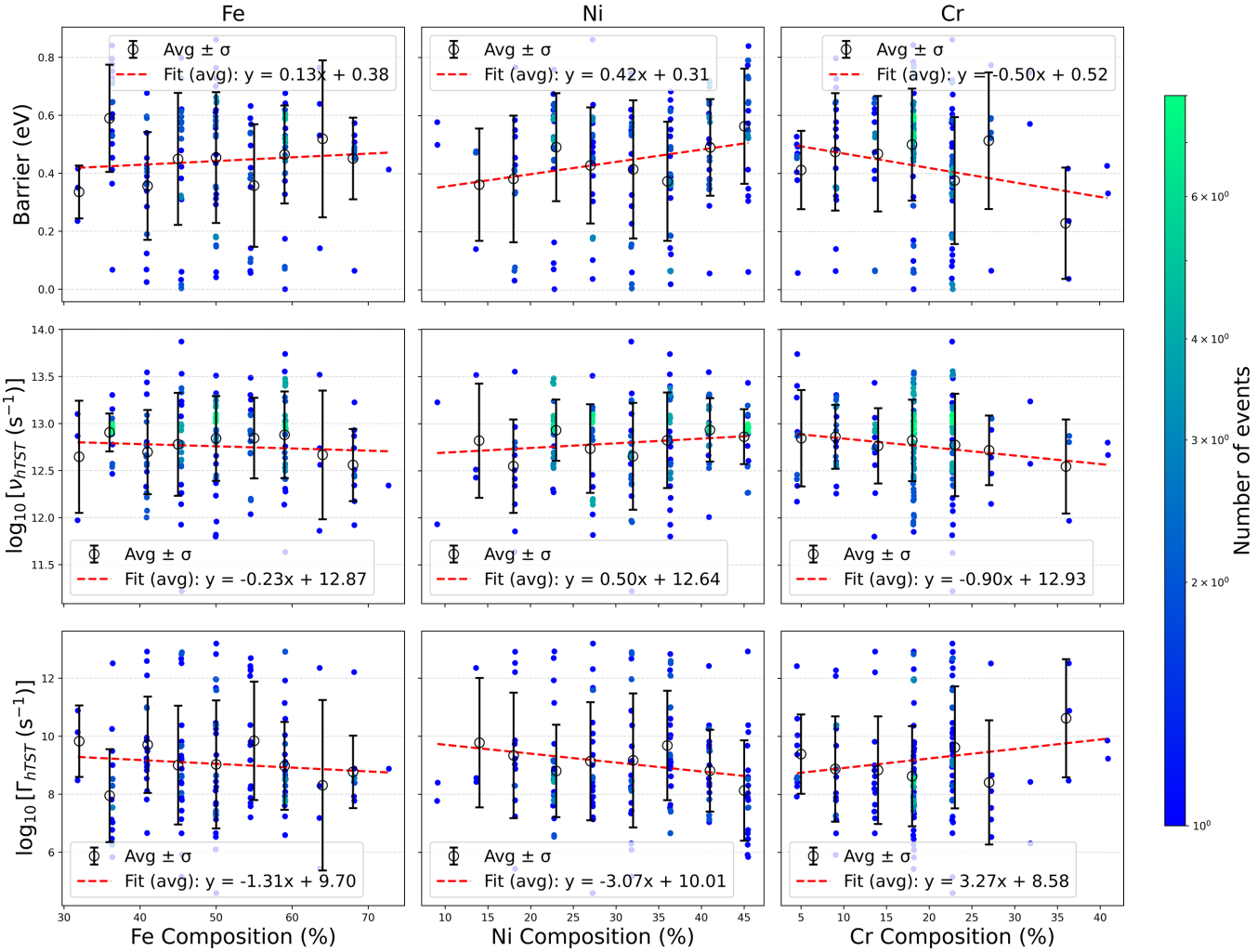

FIG. 18. Correlation between vacancy cluster migration properties and local first-nearest-neighbor (1NN) atomic compositions during 3V(3,0,0,0,0,0) → 3V(2,1,0,0,0,0) migration of a trivacancy cluster. The rows correspond to: (top) migration barrier energy (eV), (middle) logarithm of the hTST prefactor ($\log_{10}[\nu_{\mathrm{hTST}}\ \mathrm{s}^{-1}]$), and (bottom) logarithm of the hTST rate ($\log_{10}[\Gamma_{\mathrm{hTST}}\ \mathrm{s}^{-1}]$) at 600 K. Columns correspond to the elemental composition fractions of Fe, Ni, and Cr in the initial-state 1NN shell surrounding the migrating cluster. The x axis shows the atomic percentage of each element in the specified environment (0–100%), and the y axis corresponds to the migration property. Individual points represent distinct migration events. Duplicate events—defined by identical local compositions (rounded to 10^{-2}) and differences smaller than 0.01 in the migration barrier (eV), $\log_{10}\nu_{\mathrm{hTST}}$, and $\log_{10}\Gamma_{\mathrm{hTST}}$—were removed. Point colors indicate the number of events in each composition–property bin using logarithmic normalization (bin widths: 1 at.% in composition; 0.02 eV for barriers; 0.10 for $\log_{10}\nu_{\mathrm{hTST}}$ and $\log_{10}\Gamma_{\mathrm{hTST}}$). Open gray circle with error bars denote the mean ± one standard deviation for each composition bin containing at least three events. Dashed red lines show linear least-squares fits performed on the binned averages, expressed as $y = \mathrm{slope} \times x + \mathrm{intercept}$, where x is the composition scaled from 0 to 1, and the slope units correspond to the property: eV per fraction for migration barriers, $\log_{10}(\mathrm{s}^{-1})$ per fraction for hTST prefactors, and $\log_{10}(\mathrm{s}^{-1})$ per fraction for hTST rates.

barrier effect or reinforcing it through a prefactor increase. Increasing the Fe concentration again exhibits weaker and more compensated behavior, with barrier and prefactor variations tending to offset one another and resulting in comparatively modest net changes in migration rates relative to the pronounced Ni-inhibiting and Cr-enhancing effects.

Figure 20 shows that composition-dependent effects persist for tetravacancy migration, although their influence on mobility is reduced compared to smaller clusters. Increasing the Ni concentration continues to suppress migration primarily through barrier increases, with prefactor changes generally acting in the same or a neutral direction. Increasing the Cr concentration remains associated with lower migration barriers and enhanced transition rates; however, the magnitude of this enhancement is diminished relative to di- and trivacancies. This reduced sensitivity reflects the increased structural stability of tetravacancies and the tendency for migration to proceed through a more limited subset of kinetically accessible pathways. Increasing the Fe concentration again produces weak and partially compensated effects, leading to only modest changes in tetravacancy migration rates.

In summary, the local chemical composition of the 1NN shell surrounding a migrating vacancy cluster plays a decisive role in controlling migration kinetics in FeNiCr concentrated solid solutions. Increasing the Ni concentration systematically stabilizes vacancy clusters against migration by raising activa-

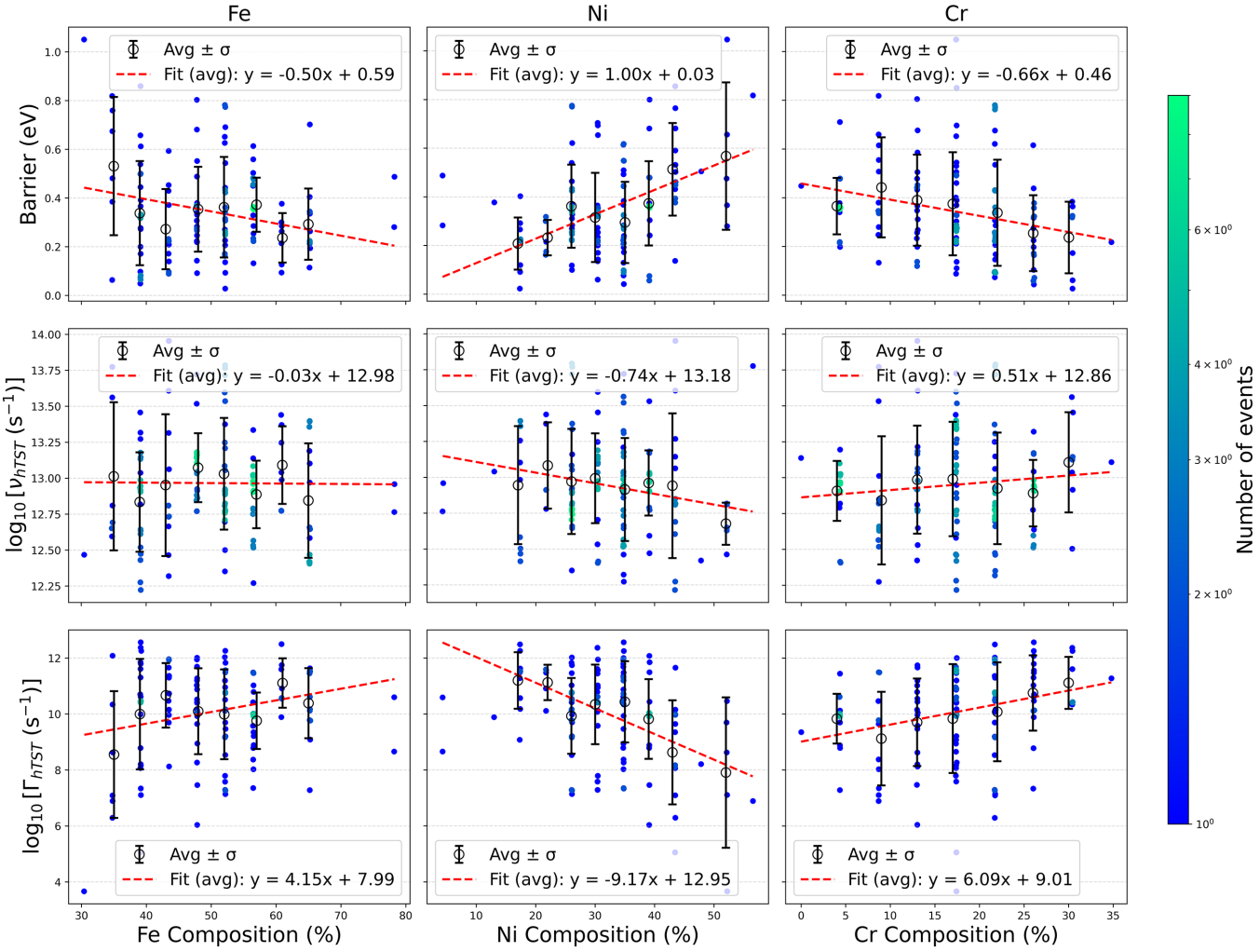

FIG. 19. Correlation between vacancy cluster migration properties and local first-nearest-neighbor (1NN) atomic compositions during 3V(2,1,0,0,0,0) → 3V(3,0,0,0,0,0) migration of a trivacancy cluster. The rows correspond to: (top) migration barrier energy (eV), (middle) logarithm of the hTST prefactor ($\log_{10}[\nu_{\mathrm{hTST}}\ \mathrm{s}^{-1}]$), and (bottom) logarithm of the hTST rate ($\log_{10}[\Gamma_{\mathrm{hTST}}\ \mathrm{s}^{-1}]$) at 600 K. Columns correspond to the elemental composition fractions of Fe, Ni, and Cr in the initial-state 1NN shell surrounding the migrating cluster. The x axis shows the atomic percentage of each element in the specified environment (0–100%), and the y axis corresponds to the migration property. Individual points represent distinct migration events. Duplicate events—defined by identical local compositions (rounded to 10^{-2}) and differences smaller than 0.01 in the migration barrier (eV), $\log_{10}\nu_{\mathrm{hTST}}$, and $\log_{10}\Gamma_{\mathrm{hTST}}$—were removed. Point colors indicate the number of events in each composition–property bin using logarithmic normalization (bin widths: 1 at.% in composition; 0.02 eV for barriers; 0.10 for $\log_{10}\nu_{\mathrm{hTST}}$ and $\log_{10}\Gamma_{\mathrm{hTST}}$). Open gray circle with error bars denote the mean ± one standard deviation for each composition bin containing at least three events. Dashed red lines show linear least-squares fits performed on the binned averages, expressed as $y = \text{slope} \times x + \text{intercept}$, where x is the composition scaled from 0 to 1, and the slope units correspond to the property: eV per fraction for migration barriers, $\log_{10}(\mathrm{s}^{-1})$ per fraction for hTST prefactors, and $\log_{10}(\mathrm{s}^{-1})$ per fraction for hTST rates.

tion barriers, whereas increasing the Cr concentration lowers barriers and enables rapid cluster motion across cluster sizes and configurations. Increasing the Fe concentration produces intermediate, partially compensated effects. This chemically driven hierarchy provides a coherent mechanistic framework for understanding vacancy-cluster migration and defect kinetics in concentrated solid solutions.

D. Lifetime and effective diffusion coefficients

To understand the dynamics of vacancy clusters in FeNiCr concentrated solid solutions, we evaluate their thermal lifetimes and effective diffusion coefficients at 600 K using a mean-field Markov chain approach (Sec. II F). Direct computation of lifetimes and mobilities from kART simulations is prohibitively expensive owing to the large variability of local chemical environments, so the mean-field Markov chain framework is adopted to efficiently sample cluster trajectories while retaining mechanism-specific kinetic statistics. In this approach, clusters are evolved stochastically until dissociation occurs at the fourth-nearest-neighbor (4NN) distance. Because clusters exist only for finite times, we report an effective diffusion coefficient D_{eff}, which reflects the transport capacity of the defect species while maintaining its

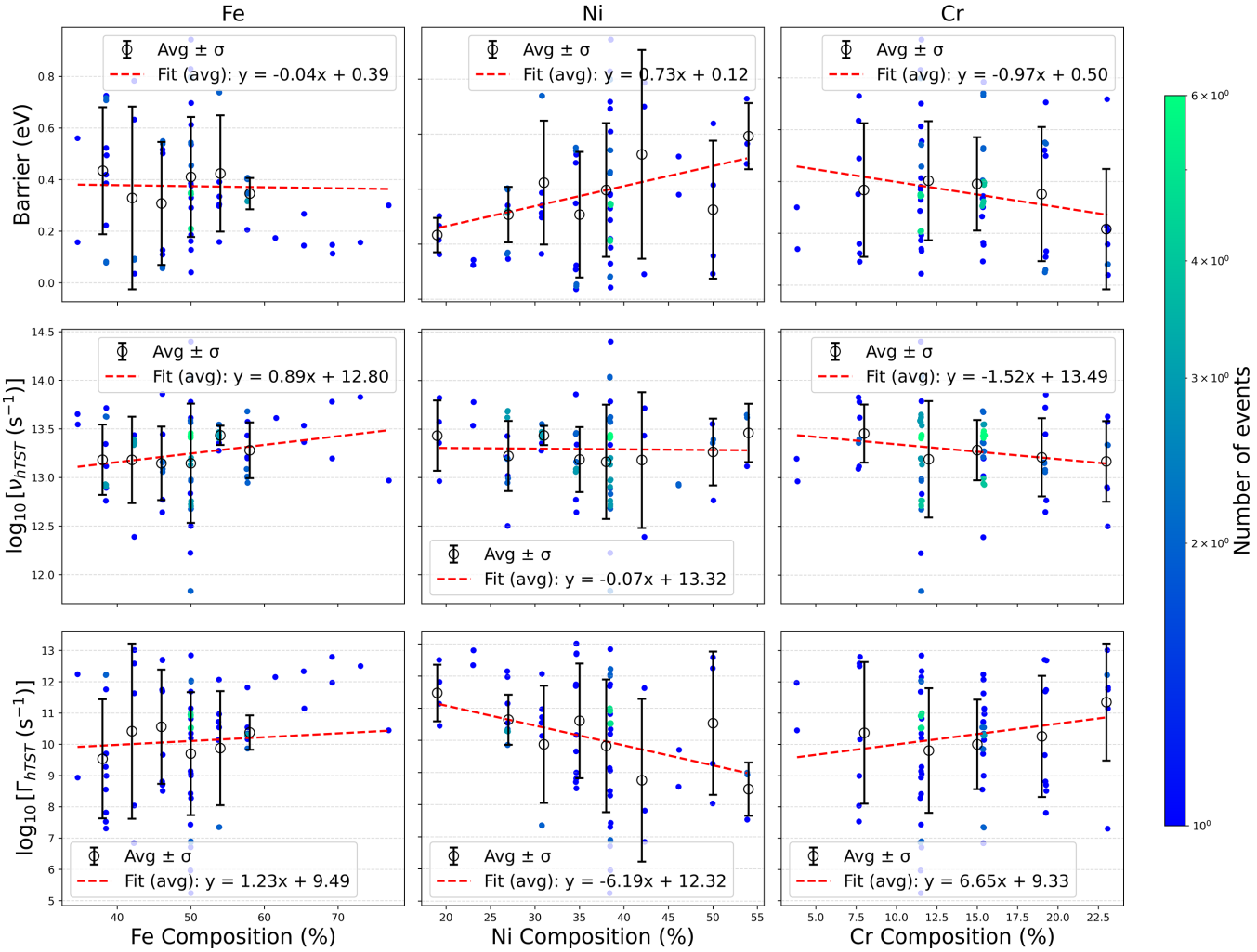

FIG. 20. Correlation between vacancy cluster migration properties and local first-nearest-neighbor (1NN) atomic compositions during 4V(5,1,0,0,0,0) → 4V(5,1,0,0,0,0) migration of a tetravacancy cluster. The rows correspond to: (top) migration barrier energy (eV), (middle) logarithm of the hTST prefactor ($\log_{10}[\nu_{\mathrm{hTST}}\ \mathrm{s}^{-1}]$), and (bottom) logarithm of the hTST rate ($\log_{10}[\Gamma_{\mathrm{hTST}}\ \mathrm{s}^{-1}]$) at 600 K. Columns correspond to the elemental composition fractions of Fe, Ni, and Cr in the initial-state 1NN shell surrounding the migrating cluster. The x axis shows the atomic percentage of each element in the specified environment (0–100%), and the y axis corresponds to the migration property. Individual points represent distinct migration events. Duplicate events—defined by identical local compositions (rounded to 10^{-2}) and differences smaller than 0.01 in the migration barrier (eV), $\log_{10}\nu_{\mathrm{hTST}}$, and $\log_{10}\Gamma_{\mathrm{hTST}}$—were removed. Point colors indicate the number of events in each composition–property bin using logarithmic normalization (bin widths: 1 at.% in composition; 0.02 eV for barriers; 0.10 for $\log_{10}\nu_{\mathrm{hTST}}$ and $\log_{10}\Gamma_{\mathrm{hTST}}$). Open gray circle with error bars denote the mean ± one standard deviation for each composition bin containing at least three events. Dashed red lines show linear least-squares fits performed on the binned averages, expressed as $y = \text{slope} \times x + \text{intercept}$, where x is the composition scaled from 0 to 1, and the slope units correspond to the property: eV per fraction for migration barriers, $\log_{10}(\mathrm{s}^{-1})$ per fraction for hTST prefactors, and $\log_{10}(\mathrm{s}^{-1})$ per fraction for hTST rates.

structural integrity, rather than a macroscopic tracer diffusion coefficient.

Table II summarizes the results for two kinetic models. In the hTST-refined model, transition rates for each migration mechanism are calculated from the sampled barriers using mechanism-specific vibrational prefactors, explicitly accounting for local environment variations and entropy effects. For each mechanism, the mean rate of the resulting rate distribution is used in the Markov simulations, while simulations with the mean rate $\pm 1\sigma$ quantify sensitivity to local chemical variability. In this framework, divacancies have lifetimes $(6.0 \pm 4.3) \times 10^{-5}$ s and diffusion coefficient $(4.4 \pm 3.4) \times 10^{10}$ Å^2 s^{-1}. Trivacancies are short lived, $(1.1 \pm 1.3) \times 10^{-9}$ s, but highly mobile, $(1.4 \pm 1.2) \times 10^{11}$ Å^2 s^{-1}, while tetravacancies have comparable lifetimes, $(1.3 \pm 1.2) \times 10^{-8}$ s, with lower mobility, $(4.6 \pm 3.8) \times 10^{9}$ Å^2 s^{-1}. In the constant-prefactor model, which applies a fixed attempt frequency of 10^{13} Hz to the same barrier distributions, the mean and mean $\pm 1\sigma$ rates are used in Markov simulations for direct comparison with hTST. For 2V clusters, the lifetime is about 40 times lower and the diffusion coefficient slightly lower (about 1.5 times) than the hTST prediction. Trivacancies show lifetimes roughly four times lower, while diffusion coefficients are about twice

TABLE II. Average thermal lifetimes and effective diffusion coefficients for vacancy clusters at 600 K. Transport properties are computed using a mean-field Markov chain framework, where cluster trajectories are sampled stochastically until dissociation at the fourth-nearest-neighbor distance. Transition rates are obtained from harmonic transition state theory (hTST), incorporating mechanism-specific vibrational prefactors and local environment variations. Uncertainties are calculated using transition rates adjusted by $\pm\sigma$ from the mean to reflect sensitivity to local chemical fluctuations. For comparison, a constant-prefactor model with $\nu_0 = 10^{13}$ Hz is also evaluated, providing a benchmark for the impact of explicit vibrational entropy and rate variability on cluster dynamics.

	hTST prefactor		Constant prefactor (10^{13} Hz)	
Cluster	Lifetime (s)	D_{eff} (Å^2 s^{-1})	Lifetime (s)	D_{eff} (Å^2 s^{-1})
1V		$(9.3\pm6.3) \times 10^2$		$(4.5\pm2.3) \times 10^3$
2V	$(6.0 \pm 4.3) \times 10^{-5}$	$(4.4 \pm 3.4) \times 10^{10}$	$(1.5 \pm 1.4) \times 10^{-6}$	$(2.8 \pm 2.5) \times 10^{10}$
3V	$(1.1 \pm1.3) \times 10^{-9}$	$(1.4 \pm1.2) \times 10^{11}$	$(2.7 \pm2.9) \times 10^{-10}$	$(2.8 \pm3.4) \times 10^{11}$
4V	$(1.3 \pm 1.2) \times 10^{-8}$	$(4.6 \pm 3.8) \times 10^9$	$(9.9 \pm 9.3) \times 10^{-9}$	$(3.0 \pm 1.2) \times 10^{10}$

higher than hTST. For tetravacancies, lifetimes are similar, but mobility is approximately six times higher compared to hTST. Small clusters (2–4 vacancies) display mobilities several orders of magnitude higher than isolated monovacancies (4.5×10^3 Å^2 s^{-1}). This originates from fundamental differences in dominant migration mechanisms: monovacancies diffuse through high and broadly distributed barriers (∼0.8–0.9 eV) [15], whereas clusters migrate predominantly via correlated, short-range rearrangements within compact configurations, involving fewer broken bonds and lower effective barriers (∼0.3–0.6 eV). The Arrhenius dependence of transition rates amplifies these differences, resulting in mobilities several orders of magnitude higher for small clusters. Cyclic low-barrier transitions further enhance local motion, a mechanism largely absent for isolated monovacancies.

However, their contribution to long-range mass transport is constrained by thermal stability: short lifetimes in both models imply frequent dissociation before extended diffusion occurs. Consequently, while small clusters significantly enhance short-range, transient mass redistribution, sustained long-range transport is governed by the interplay between rapid migration and thermally activated breakup. Diffusion therefore varies nonmonotonically with cluster size, reflecting the coupled roles of mobility and stability in FeNiCr alloys.

IV. DISCUSSION

In this study, we conducted an in-depth atomistic investigation of vacancy cluster behavior and diffusion in FeNiCr concentrated solid solutions (CSAs) using the off-lattice kinetic activation-relaxation technique (kART) combined with harmonic transition state theory (hTST). By examining di-, tri-, and tetravacancy clusters, we provide insights into their thermodynamic stability, kinetic mobility, and compositional dependencies, revealing critical mechanisms that govern microstructural evolution under thermal and irradiation conditions.

Our results establish a clear energetic preference for vacancy clustering in FeNiCr alloys. The formation energy per vacancy systematically decreases with increasing cluster size—from 1.65 eV for isolated vacancies to 1.30 eV for tetravacancies, indicating a strong driving force for defect agglomeration. Compact clusters such as 1NN divacancies exhibit the highest thermodynamic stability, while configurations involving greater separation between vacancies are energetically disfavored because of increased lattice distortion and reduced binding energy. These findings are consistent with experimental and theoretical observations in high-entropy and concentrated solid-solution alloys [38–41], confirming that vacancy interactions play a crucial role in microstructural evolution under irradiation and high-temperature conditions.

Local chemical composition significantly affects stability. A strong negative correlation exists between the Ni content and vacancy formation energy across all cluster types, confirming Ni's role in stabilizing vacancy clusters by lowering formation energies. Ni concentration rises from 28% in the bulk to as high as 42.3% near certain trivacancy configurations, promoting energetically favorable clustering. In contrast, Fe shows a positive correlation with formation energy, making Fe-rich environments less favorable for vacancy clustering. Cr's effect is more complex: it aids strain relief in smaller clusters but destabilizes larger ones, showing weaker or positive correlations with formation energy. These trends align with density functional theory studies, which note Ni's stabilizing effect and the destabilizing influence of Fe and Cr in Fe-Cr-Ni systems [14,42]. Ni enrichment near vacancy clusters further supports its role in enhancing defect stability, while Fe's larger atomic size likely increases strain, contributing to its destabilizing effect.

The kinetic behavior of vacancy clusters is governed by migration energy barriers, diffusion prefactors, and transition rates, all influenced by local atomic environments. A consistent pattern emerges: low-energy barriers (0.3–0.6 eV) correspond to high prefactors (10^{13}–10^{14}s^{-1}), indicating minimal entropic penalties for compact configurations, while higher barriers (0.9–1.2 eV) align with lower prefactors (10^{12}–10^{13} s^{-1}), reflecting greater entropic costs for extended structures. This pattern is most evident for divacancies, where the 1NN to 1NN transition dominates because of a low barrier (0.43 ± 0.11 eV), high prefactor (1.07×10^{13} s^{-1}), and robust transition rate (1.35×10^9 s^{-1}). This indicates that divacancy migration primarily occurs through short-range jumps, with long-range transitions (e.g., 1NN to 4NN) being less frequent because of higher barriers (0.72 eV) and lower rates (8.92×10^6 s^{-1}). Trivacancy clusters exhibit similarly high mobility through frequent transitions between compact configurations, with barriers in the range 0.28–0.67 eV and transition rates reaching 1.87×10^{12} s^{-1}. Tetravacancy clusters preferentially

undergo self-transitions within compact arrangements, characterized by moderate activation barriers (0.35–0.71 eV) and high transition rates of up to 8.8×10^{12} s^{-1}. In contrast, extended tetravacancy transitions involve substantially higher barriers ($\gtrsim$1.0 eV), which strongly suppress long-range migration and promote spatial localization.

Analysis at the level of individual atomic transitions identifies the atomic species that preferentially mediate vacancy–cluster motion within the bound-state network. For divacancies, the dominant 1NN $\rightarrow$ 1NN mechanism exhibits a lower selective migration barrier for Cr ($\sim$0.32 eV) than for Fe ($\sim$0.48 eV), resulting in Cr-mediated transition rates on the order of 10^{10} s^{-1}. Similar behavior is observed for trivacancies, where Cr-mediated transitions display barriers of $\sim$0.32–0.37 eV and transition rates approaching 10^{10} s^{-1}, exceeding those associated with Fe- and Ni-mediated pathways. For tetravacancies, short-range Cr-mediated transitions again show the lowest barriers ($\sim 0.28 - 0.34$ eV) and the highest rates ($\sim 10^{10}$–10^{11} s^{-1}), whereas Fe-mediated transitions remain comparatively slow. While these findings characterize event-level mediation within vacancy–cluster dynamics rather than macroscopic tracer diffusion, they clearly demonstrate that local chemical identity—particularly the presence of Cr—plays a dominant role in the vacancy–cluster migration kinetics.

The influence of local chemical composition on vacancy-cluster migration in FeNiCr concentrated solid solutions is characterized by a barrier-dominated dependence on the initial-state local environment across all cluster sizes. Compositional sensitivity analysis reveals that chromium enrichment around vacancies consistently facilitates rapid cluster motion by substantially reducing migration barriers (-0.85 eV per atomic fraction for divacancies, up to -0.66 eV for trivacancies, and -0.97 eV for tetravacancies), producing large rate enhancements ($+6.92$, $+6.09$, and $+6.65 \log_{10} \Gamma$ per fraction Cr for di-, tri-, and tetravacancies, respectively). In contrast, nickel exerts a robust inhibiting effect by increasing activation barriers, with slopes ranging from $+0.39$ eV per fraction for divacancies to as high as $+1.00$ eV for asymmetric trivacancy migration, thereby suppressing transition rates by up to $-9.17 \log_{10} \Gamma$. Iron generally exhibits intermediate behavior, acting as a promoter in divacancy and asymmetric trivacancy pathways with barrier reductions of -0.19 and -0.50 eV per fraction, respectively, yielding corresponding rate enhancements of $+0.54$ and $+4.15 \log_{10} \Gamma$. However, for symmetric trivacancy transitions $[3V(3, 0, 0, 0, 0, 0) \rightarrow 3V(3, 0, 0, 0, 0, 0)]$, iron uniquely acts as a weak inhibitor, raising barriers by $+0.19$ eV per fraction and suppressing rates by -1.26 $\log_{10} \Gamma$. In tetravacancy self-transitions $[4V(5, 1, 0, 0, 0, 0) \rightarrow 4V(5, 1, 0, 0, 0, 0)]$, iron's influence remains negligible with a barrier slope of only -0.04 eV per fraction and a minor rate slope of $+1.23$ $\log_{10} \Gamma$. These systematic trends suggest that chromium creates favorable energy landscapes likely by minimizing local strain, while nickel's stronger bonding and configurational stabilization increase the energetic penalties for migration, establishing a coherent, chemically driven hierarchy for defect kinetics in these complex alloys.

Vacancy cluster lifetimes and diffusion coefficients provide key insight into their dynamics. We quantify these for small clusters in FeNiCr at 600 K using a mean-field Markov chain with hTST-derived rates. Divacancies exhibit lifetimes around 6×10^{-5} s and effective diffusion coefficients of 4.4×10^{10} Å^2/s, showing high stability and mobility through correlated, short-range jumps. Trivacancies (3V) are highly mobile (1.4×10^{11} Å^2/s) but very short lived ($\sim 10^{-9}$ s), while tetravacancies (4V) have moderate mobility (4.6×10^9 Å^2/s) and lifetimes of $\sim 10^{-8}$ s. Compared to isolated monovacancies (9.3×10^2 Å^2/s), these clusters are several orders of magnitude more mobile, driven by lower effective migration barriers (0.3–0.6 eV) and compact, correlated rearrangements. Cyclic, low-barrier transitions further enhance short-range motion, though frequent dissociation events limit long-range transport. Consequently, small clusters contribute primarily to transient mass redistribution rather than sustained diffusion, highlighting that mobility and stability must be treated together when modeling defect evolution in concentrated alloys.

These findings have important implications for understanding defect dynamics in FeNiCr concentrated solid solutions used in extreme environments, such as nuclear and aerospace applications. The relatively high mobility of di- and trivacancy clusters indicates that these defects can contribute significantly to short-range mass transport and local defect redistribution under nonequilibrium conditions. In contrast, the reduced propensity for long-range migration observed for tetravacancy clusters suggests a tendency toward spatial localization, which may influence the evolution of vacancy aggregation and microstructural heterogeneity. The compositional dependence, particularly Ni's stabilization of vacancy clusters and Cr's promotion of mobility, indicates that tailoring alloy composition (e.g., increasing Ni or Cr content in specific regions) could optimize defect dynamics for specific applications.

In summary, this study reveals the critical interplay between cluster size, local composition, and diffusion kinetics in FeNiCr CSAs. By integrating kART and hTST, we offer a robust framework for understanding defect evolution, providing actionable insights for designing advanced materials with superior radiation resistance and thermal stability.

V. CONCLUSIONS

This investigation into vacancy cluster dynamics in FeNiCr concentrated solid solutions (CSAs) using the kinetic activation-telaxation technique (kART) and harmonic transition state theory (hTST) reveals critical insights into their thermodynamic stability and kinetic behavior. The study demonstrates that vacancy cluster stability increases with size, driven by reduced formation energies and influenced significantly by local chemical composition, particularly Ni's stabilizing effect and Cr's role in modulating mobility. Divacancies combine notable stability with substantial mobility, enabling efficient long-range diffusion before dissociation. Trivacancies, despite their reduced stability, exhibit exceptional mobility, making them dominant contributors to rapid defect recombination processes. In contrast, tetravacancies demonstrate greater stability but significantly restricted mobility, influencing localized defect interactions and microstructural evolution. These findings underscore the pivotal role of compositional tuning in controlling defect evolution, through changes both in the energy and entropy of diffusion, with Ni enhancing stability and Cr promoting diffusion. The

results provide a robust framework for understanding microstructural evolution in FeNiCr CSAs under thermal and irradiation conditions, offering actionable strategies for alloy design. By tailoring the Ni and Cr concentrations, material scientists can optimize defect dynamics to enhance radiation tolerance and thermal stability, critical for applications in nuclear reactors and aerospace systems. This work not only advances the fundamental understanding of defect interactions in complex alloys but also paves the way for predictive modeling and the development of next-generation materials capable of withstanding extreme environments. Future studies should explore the interplay of vacancy clusters with other defects, such as interstitials, and validate these findings through experimental techniques like positron annihilation spectroscopy to further refine alloy performance.

ACKNOWLEDGMENTS

This work was supported in part by the Materials Ageing Institute Scientific Network (MAI-SN). G.A. and C.D. acknowledge the collaboration within the framework of the INNUMAT project, funded by the European Union. This work was carried out without direct financial support from the project. M.M.R. acknowledges partial support from the Trottier Family Foundation. N.M. acknowledges partial support through a Discovery grant from the Natural Science and Engineering Research Council of Canada. We are grateful to Calcul Québec and the Digital Research Alliance of Canada for generous allocation of computational resources.

DATA AVAILABILITY

The most recent packages for k-ART and ARTn are available freely upon request. Please contact Normand Mousseau [43]. The data that support the findings of this article are not publicly available because they contain commercially sensitive information. The data are available from the authors upon reasonable request.

[1] J. W. Yeh, S. K. Chen, S. J. Lin, J.-Y. Gan, T.-S. Chin, T.-T. Shun, C.-H. Tsau, and S.-Y. Chang, Nanostructured high-entropy alloys with multiple principal elements: Novel alloy design concepts and outcomes, Adv. Eng. Mater. **6**, 299 (2004).

[2] B. Cantor, I. T. H. Chang, P. Knight, and A. J. B. Vincent, Microstructural development in equiatomic multicomponent alloys, Mater. Sci. Eng. A **375-377**, 213 (2004).

[3] E. P. George, D. Raabe, and R. O. Ritchie, High-entropy alloys, Nat. Rev. Mater. **4**, 515 (2019).

[4] D. B. Miracle and O. N. Senkov, A critical review of high entropy alloys and related concepts, Acta Mater. **122**, 448 (2017).

[5] S. J. Zinkle and G. S. Was, Materials challenges in nuclear energy, Acta Mater. **61**, 735 (2013).

[6] G. S. Was, *Fundamentals of Radiation Materials Science: Metals and Alloys* (Springer, New York, 2016).

[7] L. K. Mansur, Theory and experimental background on dimensional changes in irradiated alloys, J. Nucl. Mater. **216**, 97 (1994).

[8] K. Nordlund, S. J. Zinkle, A. E. Sand, F. Granberg, R. S. Averback, R. E. Stoller, T. Suzudo, L. Malerba, F. Banhart, W. J. Weber, *et al.*, Primary radiation damage: A review of current understanding and models, J. Nucl. Mater. **512**, 450 (2018).

[9] S. I. Golubov, B. N. Singh, and H. Trinkaus, Defect accumulation in FCC and BCC metals under irradiation, J. Nucl. Mater. **276**, 78 (2000).

[10] C. Cawthorne and E. J. Fulton, Voids in irradiated stainless steel, Nature (London) **216**, 575 (1967).

[11] G. R. Odette and G. E. Lucas, Irradiation embrittlement of reactor pressure vessel steels: Mechanisms, models, and data, JOM **60**, 44 (2008).

[12] G. J. Ackland, Controlling radiation damage, Science **327**, 1587 (2010).

[13] L. Delczeg, B. Johansson, and L. Vitos, *Ab initio* description of monovacancies in paramagnetic austenitic Fe-Cr-Ni alloys, Phys. Rev. B **85**, 174101 (2012).

[14] A. Manzoor, Y. Zhang, and D. S. Aidhy, Factors affecting the vacancy formation energy in $Fe_{70}Ni_{10}Cr_{20}$ random concentrated alloy, Comput. Mater. Sci. **198**, 110669 (2021).

[15] J. Lefèvre López, N. Mousseau, G. Adjanor, and C. Domain, Harmonic transition state theory applied to vacancy diffusion pre-exponential factors in a concentrated solid-solution alloy, Phys. Rev. Mater. **8**, 013609 (2024).

[16] A. Sauvé-Lacoursière, S. Gelin, G. Adjanor, C. Domain, and N. Mousseau, Unexpected role of prefactors in defects diffusion: The case of vacancies in the 55Fe−28Ni−17Cr concentrated solid-solution alloys, Acta Mater. **237**, 118153 (2022).

[17] G. Adjanor, R. Vasav, T. Jourdan, C. Domain, N. Mousseau, M. M. Rahman, M. Athènes, Overview of kinetic Monte Carlo methods used to simulate microstructural evolution of materials under irradiation, EPJ Nuclear Sci. Technol. **11**, 64 (2025).

[18] F. El-Mellouhi, N. Mousseau, and L. J. Lewis, Kinetic activation-relaxation technique: An off-lattice self-learning kinetic Monte Carlo algorithm, Phys. Rev. B **78**, 153202 (2008).

[19] L. K. Béland, P. Brommer, F. El-Mellouhi, J.-F. Joly, and N. Mousseau, Kinetic activation-relaxation technique, Phys. Rev. E **84**, 046704 (2011).

[20] N. Mousseau, L. K. Béland, P. Brommer, F. El-Mellouhi, J. F. Joly, G. K. N'tsouaglo, O. A. Restrepo, and M. Trochet, Following atomistic kinetics on experimental timescales with the kinetic activation relaxation technique, Comput. Mater. Sci. **100**, 111 (2015).

[21] M. M. Rahman, F. El-Mellouhi, and N. Mousseau, Structural evolution of vacancy clusters in α-iron: A kinetic activation-relaxation technique study, Phys. Rev. Mater. **7**, 093602 (2023).

[22] M. M. Rahman, F. El-Mellouhi, O. Bouhali, C. S. Becquart, and N. Mousseau, Pressure effect on diffusion of carbon at the $85.91^\circ\langle 100\rangle$ symmetric tilt grain boundary of α-iron, Phys. Rev. Mater. **5**, 043605 (2021).

[23] L. K. Béland, P. Brommer, J.-F. Joly, and N. Mousseau, Understanding long-time vacancy aggregation in iron: A kinetic

activation-relaxation technique study, Phys. Rev. B **84**, 054106 (2011).

[24] G. H. Vineyard, Frequency factors and isotope effects in solid state rate processes, J. Phys. Chem. Solids **3**, 121 (1957).

[25] S. Gelin, A. Champagne-Ruel, and N. Mousseau, Enthalpy-entropy compensation of atomic diffusion originates from softening of low frequency phonons, Nat. Commun. **11**, 3977 (2020).

[26] M. M. Rahman, Modeling and numerical study of the diffusion of point defects in α- iron, Ph.D. thesis, University of Montreal, 2023.

[27] B. D. McKay and A. Piperno, Practical graph isomorphism, ii, J. Symb. Comput. **60**, 94 (2014).

[28] G. Barkema and N. Mousseau, Event-based relaxation of continuous disordered systems, Phys. Rev. Lett. **77**, 4358 (1996).

[29] R. Malek and N. Mousseau, Dynamics of Lennard-Jones clusters: A characterization of the activation-relaxation technique, Phys. Rev. E **62**, 7723 (2000).

[30] A. Jay, C. Huet, N. Salles, M. Gunde, L. Martin-Samos, N. Richard, G. Landa, V. Goiffon, S. de Gironcoli, A. Hemeryck, and N. Mousseau, Finding reaction pathways and transition states: R-ARTn and d-ARTn as an efficient and versatile alternative to string approaches, J. Chem. Theory Comput. **16**, 6726 (2020).

[31] B. Puchala, M. L. Falk, and K. Garikipati, An energy basin finding algorithm for kinetic Monte Carlo acceleration, J. Chem. Phys. **132**, 134104 (2010).

[32] G. Bonny, N. Castin, and D. Terentyev, Interatomic potential for studying ageing under irradiation in stainless steels: The FeNiCr model alloy, Modell. Simul. Mater. Sci. Eng. **21**, 085004 (2013).

[33] T. P. C. Klaver, D. J. Hepburn, and G. J. Ackland, Defect and solute properties in dilute Fe-Cr-Ni austenitic alloys from first principles, Phys. Rev. B **85**, 174111 (2012).

[34] C. Zhang, X. Cao, Y. Li, S. Jin, E. Lu, H. Tian, P. Zhang, and B. Wang, Thermal evolution of vacancy-type defects in quenched FeCrNi alloys, Appl. Phys. A **119**, 1431 (2015).

[35] M. Benkaddour, D. Bahia, A. Benkaddour, and J. Barkani, Assessment of vacancy migration energy in a ternary austenitic steel Fe–Cr-Ni with 16% chromium and 20% nickel composition, using kinetic Monte Carlo method, considering an ordering model via vacancy diffusion mechanism, Interactions **245**, 232 (2024).

[36] M. Grabowski, J. Rogal, and R. Drautz, Kinetic Monte Carlo simulations of vacancy diffusion in nondilute Ni-X (X = Re, W, Ta) alloys, Phys. Rev. Mater. **2**, 123403 (2018).

[37] See Supplemental Material at http://link.aps.org/supplemental/10.1103/p14c-288d for additional figures and tables presenting detailed migration barriers, harmonic transition state theory (hTST) prefactors, transition rates, and alternative vacancy-cluster diffusion mechanisms for divacancy, trivacancy, and tetravacancy configurations in Fe–Ni–Cr concentrated solid-solution alloys. Tables S1–S3 and Figs. S1–S3 are appropriately cited in the manuscript.

[38] Z. Wang, C. Liu, and P. Dou, Thermodynamics of vacancies and clusters in high-entropy alloys, Phys. Rev. Mater. **1**, 043601 (2017).

[39] Y. Harada and K. Tanabe, Energetics of vacancy clusters in TiVTaW low-activation high-entropy alloy investigated by *ab initio* calculations, Fusion Eng. Des. **209**, 114711 (2024).

[40] C. Lu, L. Niu, N. Chen, K. Jin, T. Yang, P. Xiu, Y. Zhang, F. Gao, H. Bei, S. Shi, *et al.*, Enhancing radiation tolerance by controlling defect mobility and migration pathways in multicomponent single-phase alloys, Nat. Commun. **7**, 13564 (2016).

[41] Z. Luo, W. Gao, and Q. Jiang, Determinants of vacancy formation and migration in high-entropy alloys, Sci. Adv. **11**, eadr4697 (2025).

[42] J. Piochaud, T. Klaver, G. Adjanor, P. Olsson, C. Domain, and C. Becquart, First-principles study of point defects in an FCC Fe-10Ni-20Cr model alloy, Phys. Rev. B **89**, 024101 (2014).

[43] normand.mousseau@umontreal.ca.